
This manuscript is a preprint and has been submitted for publication in **Earth and Planetary Science Letters**. Please note that this version of the manuscript has undergone peer-review but has not yet been accepted for publication. Subsequent versions of the manuscript may have slightly different content. If accepted, the final version of this manuscript will be available via the “Peer-reviewed Publication” DOI link on the right-hand side of this webpage. Please feel free to contact any of the authors directly to comment on the manuscript.

October 26th, 2021

1 **Field evidence for disequilibrium dynamics in preserved fluvial cross-strata: A**
2 **record of discharge variability or morphodynamic hierarchy?**

3 *Sinéad J. Lyster^{1*}, Alexander C. Whittaker¹, Elizabeth A. Hajek² and Vamsi Ganti^{3,4}*

4 ¹*Department of Earth Science and Engineering, Imperial College London, London, UK.*

5 ²*Department of Geosciences, The Pennsylvania State University, Pennsylvania, USA.*

6 ³*Department of Geography, University of California Santa Barbara, California, USA.*

7 ⁴*Department of Earth Science, University of California Santa Barbara, California, USA.*

8 **s.lyster17@imperial.ac.uk*

9 **Abstract**

10 Bedforms preserved in the rock record can provide detailed information on the morphologies
11 and hydrodynamics of ancient fluvial systems on Earth and other planets. Existing process–
12 product relations for bedform preservation assume that fluvial cross strata reflect conditions
13 under which bedforms were equilibrated with the prevailing flow, i.e., steady-state
14 conditions. However, recent theoretical and experimental observations indicate that
15 enhanced bedform preservation can occur in non-steady state, or disequilibrium, conditions,
16 and it is currently unclear how prevalent disequilibrium dynamics are in preserved fluvial
17 strata at outcrop scale. Here we explore whether steady-state assumptions are appropriate
18 for ancient fluvial systems by evaluating the nature of bedform preservation in well studied
19 fluvial deposits of three Late Cretaceous (Turonian and Campanian) geologic formations in
20 central Utah, USA: the Blackhawk Formation, Castlegate Sandstone, and Ferron Sandstone. In
21 the field, we made systematic measurements of dune-scale cross-strata to quantify the extent
22 to which preserved cross-sets reflect dune preservation in steady-state conditions. Across the
23 three formations, consistently low coefficients of variation in preserved cross-set thicknesses
24 of 0.25–0.5 are inconsistent with bedform preservation in steady-state conditions, and
25 instead point to fluvial systems in which enhanced bedform preservation occurred in
26 disequilibrium conditions.

27 Enhanced bedform preservation in dune-scale cross-stratification can be explained by two
28 independent hypotheses: the effect of flashy flood hydrographs on bedform preservation
29 (flood hypothesis) or bedform preservation in the presence of larger migrating barforms
30 (hierarchy hypothesis). We estimated bedform turnover timescales to quantitatively assess
31 these competing hypotheses and contextualize their implications. Under the flood
32 hypothesis, field measurements are consistent with enhanced bedform preservation driven
33 by flashy flood hydrographs with flood durations ranging on the order of hours to a few days,
34 which are consistent with perennial fluvial systems subject to heavy rains and tropical storms.
35 Alternatively, under the hierarchy hypothesis, field measurements are consistent with
36 bedform climb angles that range from 10^{-2} to 10^{-1} , reflecting rapid bar migration. Our work
37 provides a novel way of investigating fluvial discharge variability in the geologic past, and we

38 outline the potential next steps to disentangle the relative controls of flow variability and
39 hierarchy in controlling bedform preservation in ancient fluvial systems.

40 **Keywords**

41 Fluvial systems; Bedforms; Cross strata; Hydrodynamics; Morphodynamics; Discharge
42 variability

43 **1. Introduction**

44 Quantitative reconstructions of palaeohydraulics from fluvial stratigraphy complement
45 qualitative observations of sedimentary facies to build more complete pictures of palaeo-
46 landscapes on Earth and other planets. In fluvial strata, preserved bedforms, which include
47 ripples, dunes, and unit bars, are crucial to these reconstructions. Bedforms are readily
48 formed on riverbeds across a range of grain sizes (e.g., Carling, 1999; Best, 2005) and their
49 evolution generates cross-stratification — the resultant cross-strata are a fundamental
50 building block of alluvium on planetary surfaces (e.g., Allen, 1982; Edgar et al., 2018). Cross-
51 strata provide a window to formative conditions in ancient fluvial systems and are routinely
52 used to reconstruct morphologies and hydrodynamics (Holbrook & Wanas, 2014; Ganti et al.,
53 2019; Wang et al., 2020; Lyster et al., 2021); for instance, measurements of dune-scale cross-
54 set thicknesses provide a mechanism to estimate the sizes of dunes active on ancient
55 riverbeds and, therefore, palaeoflow depths (Leclair & Bridge, 2001; Bradley & Venditti,
56 2017). Moreover, bedform kinematics respond to spatial and temporal changes in flow and
57 sediment transport conditions (e.g., Ten Brinke et al., 1999; Martin & Jerolmack, 2013; Wu et
58 al., 2020), and recent research has highlighted that these changes may be recorded in
59 preserved cross-set geometries (Leary & Ganti, 2020). If we can use geometries of cross-
60 stratification to extract information about water and sediment discharge variability, this
61 would significantly improve our understanding of ancient fluvial systems, including river
62 response to climatic perturbation (e.g., Foreman et al., 2012; Colombera et al., 2017).
63 However, a crucial outstanding challenge in this field of research involves adapting
64 engineering-scale insights, which are typically founded in precisely defined boundary
65 conditions (and which underpin palaeohydraulic reconstructions), to geological scales over
66 which more variability in environmental conditions is typically assumed due to issues of time-
67 averaging and temporal incompleteness in the rock record (e.g., Romans et al., 2016; Straub
68 et al., 2020).

69 Process–product relationships between bedform evolution and cross-stratal geometries have
70 primarily been studied using small-scale physical experiments and numerical models (Paola &
71 Borgman, 1991; Bridge, 1997; Leclair, 2002; Jerolmack & Mohrig, 2005; Ganti et al., 2013; Wu
72 et al., 2020). Existing models that relate cross-set thicknesses to original bedform heights rely
73 on the assumption that the formative train of bedforms evolved in steady-state conditions
74 under no-net aggradation or with a small bedform climb angle ($<10^{-2}$; gradient in terms of y/x)

75 (Paola & Borgman, 1991; Jerolmack & Mohrig, 2005). For a range of these formative
76 conditions, theory, numerical models and experimental observations suggest the bedform
77 preservation ratio — defined as the ratio of the average preserved cross-set thicknesses and
78 the average original bedform heights — is a near-constant value of 0.3 (Paola & Borgman,
79 1991; Leclair & Bridge, 2001; Leclair, 2002; Jerolmack & Mohrig, 2005). Further, these models
80 predict that the coefficient of variation, *CV*, of cross-set thicknesses has a constant value of
81 0.88 (Paola & Borgman, 1991; Leclair & Bridge, 2001; Leclair, 2002; Jerolmack & Mohrig,
82 2005), with Bridge (1997) suggesting that the steady-state model for bedform preservation
83 can be applied so long as the *CV* of cross-set thicknesses is bounded by 0.88 ± 0.30 . While these
84 insights have primarily been supported by numerical and experimental studies under steady-
85 state conditions (e.g., Leclair, 2002; Ganti et al., 2013; Leary & Ganti, 2020), they are widely
86 applied in field-scale palaeohydrological studies (e.g., Holbrook & Wanas, 2014; Ganti et al.,
87 2019; Wang et al., 2020; Lyster et al., 2021).

88 However, steady-state conditions, strictly defined, are not commonly observed in natural
89 systems when discharge is variable (e.g., Fielding et al., 2018; Ghinassi et al., 2018; Herbert et
90 al., 2020), or under relatively constant flow conditions in which spontaneously developed
91 features, such as bars, establish complex and locally variable flow conditions that change as
92 bars shift and channels migrate (Reesink et al., 2015; Chamberlin & Hajek, 2019; Ganti et al.,
93 2020; Wysocki & Hajek, 2021). These non-steady, or disequilibrium, conditions are
94 increasingly recognized to be fundamental controls on fluvial behaviour and stratigraphic
95 architecture (Plink-Björklund, 2015; Reesink et al., 2015; Fielding et al., 2018; Ghinassi et al.,
96 2018; Ganti et al., 2020; Herbert et al., 2020; Leary & Ganti, 2020; Wysocki & Hajek, 2021). At
97 the bedform scale, recent theoretical and experimental observations indicate that fluvial
98 cross-strata may preferentially record bedform dynamics in disequilibrium conditions
99 (Reesink et al., 2015; Ganti et al., 2020; Leary & Ganti, 2020), i.e., when flow and bedform
100 evolution are out of phase (c.f. Myrow et al., 2018). Bedform disequilibrium conditions are
101 characterized by localized increase in sedimentation rates relative to bedform migration
102 rates, which enhances the preservation of bedforms (Reesink et al., 2015; Ganti et al., 2020;
103 Leary & Ganti, 2020). Cross-sets preserved in disequilibrium conditions have diagnostic
104 geometries that deviate from cross-sets preserved in steady-state conditions: a) restricted
105 range of cross-set thickness distributions such that $CV < 0.88$ and b) elevated bedform
106 preservation ratios (> 0.3) such that a larger fraction of the formative topography is preserved
107 in the stratigraphy (Jerolmack & Mohrig, 2005; Leary & Ganti, 2020; Wu et al., 2020).

108 Two distinct disequilibrium conditions lead to enhanced bedform preservation. First, Leary
109 and Ganti (2020) used experimental data to show that characteristic patterns of dune
110 preservation are found under different conditions of formative flow variability (i.e., the near-
111 instantaneous short-term discharge variability associated with the magnitudes and timescales
112 of individual floods). They demonstrated that dune preservation preferentially occurs during
113 flood recession, and that preserved cross-sets only have geometries that are consistent with
114 steady-state conditions when the formative flow duration (T_f), i.e. the flood recession, is

115 greater than the bedform turnover timescale (T_t) — defined as the time it takes to displace
116 the volume of sediment in a bedform (Myrow et al., 2018). Conversely, when the flood
117 recession is shorter than the bedform turnover timescale, the larger peak flood-equilibrated
118 dunes get abandoned and are minimally reworked during the flood recession and subsequent
119 low flow conditions, which results in a high bedform preservation ratio and low CV for
120 preserved cross-sets (Leary & Ganti, 2020). These conditions are typical in rivers with flashy
121 flood hydrographs, which are characterised by rapid flow deceleration and, therefore, short
122 flood recessions. We term this the *flood hypothesis* for enhanced bedform preservation.
123 Moreover, Leary and Ganti (2020) showed that it is possible to estimate formative flow
124 durations from preserved cross-sets — this may enable quantitative reconstructions of flood
125 variability from the rock record and augment traditional qualitative methods that rely on
126 facies and architectural models (e.g., Plink-Björklund, 2015). Alternatively, the self-
127 organization of fluvial systems into a morphodynamic hierarchy (e.g., dunes, bars, channels,
128 channel belts) can also result in enhanced preservation of the topography associated with
129 each hierarchical level (Ganti et al., 2020). In this scenario, high bedform preservation ratio
130 and low CV can occur due to localized increase in the angle of climb of bedforms associated
131 with, for example, concurrent migration of dunes and bars (Jerolmack & Mohrig, 2005; Ganti
132 et al., 2013; Reesink et al., 2015; Ganti et al., 2020), which include both unit bars and longer-
133 lived compound bar features. We term this the *hierarchy hypothesis* for enhanced bedform
134 preservation. In both of these scenarios, cross-strata are expected to encode more detailed
135 information about morphodynamic conditions in ancient fluvial systems, which are not
136 accounted for in models that assume bedform preservation occurred in steady-state
137 conditions.

138 Despite advances in understanding bedform dynamics, the prevalence of bedform
139 disequilibrium dynamics in preserved fluvial strata is currently unclear, partly because we lack
140 detailed field measurements of cross-set geometries and their statistical nature. While a
141 handful of field studies have documented low CV (0.3–0.7) in fluvial cross-strata (Jerolmack &
142 Mohrig, 2005; Colombera et al., 2017; Cardenas et al., 2020; Wang et al., 2020), consistent
143 with bedform disequilibrium dynamics, these data are usually limited to a few outcrop
144 observations for individual geologic formations. Here, we systematically characterize the
145 geometries and statistical nature of dune-scale cross-strata for three Late Cretaceous geologic
146 formations in central Utah, USA (Figs 1,2), to assess the nature of dune preservation. Across
147 all three formations, we show that dune-scale cross-strata are dominated by the preservation
148 of bedform disequilibrium dynamics, which calls into question the use of steady-state
149 assumptions in palaeohydraulic reconstructions. Using these field observations, we
150 reconstruct bedform kinematics (i.e., turnover timescales) and quantify the formative
151 conditions that are consistent with field data under both the flood and hierarchy hypotheses
152 (i.e., flood durations, migration rates). Finally, we evaluate whether it is possible to
153 deconvolve the relative roles of flow variability and morphodynamic hierarchy on enhanced
154 bedform preservation, which may provide a potentially powerful pathway to reconstruct

155 flood variability in ancient fluvial systems, and to evaluate the nature of interactions between
156 dunes, bars, channel migration and channel avulsion in palaeo-channel networks.

157 **2. Study area**

158 In the Late Cretaceous North American continent, rivers draining the Sevier orogenic fold-
159 and-thrust belt delivered sediment to the Western Interior Seaway (WIS) (e.g., Kauffman &
160 Caldwell, 1993) (Fig. 1). We focus on well-studied fluvial strata of the Late Cretaceous
161 Blackhawk Formation, Castlegate Sandstone and Ferron Sandstone in central Utah, USA (Figs
162 1,2) (c.f. Lyster et al., 2021). These strata have distinct architectures and are interpreted to
163 preserve differing fluvial styles; the Ferron Sandstone preserves major meandering trunk
164 channels (Cotter, 1971; Chidsey et al., 2004), while, at the Blackhawk–Castlegate transition,
165 single- and multi-thread channels of the Blackhawk Formation (Adams & Bhattacharya, 2005;
166 Hampson et al., 2013; Flood & Hampson, 2014) are capped by predominantly braided
167 channels of the Castlegate Sandstone (e.g., Miall, 1993, 1994) (Fig. 1,2). Moreover, these
168 systems are potentially linked with a monsoonal climate (Fricke et al., 2010; Sewall & Fricke,
169 2013).

170 **2.1 Blackhawk Formation and Castlegate Sandstone, Mesaverde Group**

171 The Campanian Blackhawk Formation and Castlegate Sandstone (Figs 1,2) represent a series
172 of transverse fluvial systems draining the Sevier orogenic front to the WIS (Pettit et al., 2019),
173 with an additional longitudinal component of drainage from the south-southwest (e.g.,
174 Szwarc et al., 2015; Pettit et al., 2019) (Fig. 1b). The lower–middle Campanian Blackhawk
175 Formation is a ledge-forming succession characterized by large fluvial channelized sandstone
176 bodies and abundant floodplain sediments (e.g., Adams & Bhattacharya, 2005; Hampson et
177 al., 2013; Flood & Hampson, 2014) (Fig. 2a–c). These sandstone bodies represent both single-
178 and multi-thread systems, as interpreted from bar architectures (Adams & Bhattacharya,
179 2005; Hampson et al., 2013). Meanwhile the middle–upper Campanian Castlegate Sandstone
180 is a cliff-forming succession situated above the Blackhawk Formation (Fig. 2a) and is
181 characterized by amalgamated fluvial channel-belt deposits, which are interpreted to
182 preserve braided rivers, and are less amalgamated in the middle with interbedded
183 mudstones, which are interpreted to preserve more sinuous/meandering channels (e.g.,
184 Miall, 1993, 1994). We collected data for the Blackhawk Formation and Castlegate Sandstone
185 from five canyons along the eastern Wasatch Plateau front (Fig. 1a; c.f. Lyster et al. (2021)).
186 Dune-scale cross-strata in the Blackhawk Formation are generally associated with bar
187 deposits, as well as lower bar, channel floor or thalweg deposits, whereas dune-scale cross-
188 strata in the Castlegate Sandstone are predominantly associated with bar deposits (Miall,
189 1993, 1994; Adams & Bhattacharya, 2005; Hampson et al., 2013; Flood & Hampson, 2014).

190 **2.2 Ferron Sandstone, Mancos Shale**

191 The Turonian Ferron Sandstone comprises three deltaic clastic wedges (Cotter, 1971; Chidsey
192 et al., 2004) (Fig. 1b). These deltas were fed by rivers draining the Sevier orogenic front to the
193 WIS and may have also featured an additional/intermittent longitudinal component of
194 drainage from the south-southwest, as observed for the Blackhawk Formation–Castlegate
195 Sandstone succession (e.g., Szwarc et al., 2015; Pettit et al., 2019). We focus on the Last
196 Chance deltaic complex, using data from three canyons in southwestern Castle Valley (Fig. 1).
197 These canyons preserve the most palaeo-landward terrestrial fluvial facies of the Last Chance
198 delta and are characterized by major channelized sandstone bodies and abundant floodplain
199 sediments and palaeosols (Cotter, 1971; Chidsey et al., 2004) (Fig. 2d–f). These strata preserve
200 the major meandering trunk channels that fed the Last Chance delta, which is evidenced by
201 abundant laterally accreted point bar deposits (Cotter, 1971; Chidsey et al., 2004) (Fig. 2f).
202 Dune-scale cross-strata in the Ferron Sandstone are generally associated with point bar
203 deposits, as well as lower bar, channel floor or thalweg deposits (Cotter, 1971; Chidsey et al.,
204 2004).

205 3. Methods

206 At field localities, we measured the geometries of dune-scale cross-sets. Trough and planar
207 cross-sets occurred predominantly in sand-grade sediments and occasionally in coarser
208 granule-grade sediments (Fig. 3). To measure the distribution of thicknesses within individual
209 cross-sets we delineated cross-set boundaries (i.e., the lower, asymptotic bounding surface
210 and the upper, erosional bounding surface) and measured cross-set thickness with a vertical
211 precision of ± 5 mm at regular intervals along the entire width of the cross-set dip-section
212 ($n=5-15$ measurements) (Fig. 3e,f), in line with methods outlined in Paola and Borgman
213 (1991), Ganti et al. (2019) and Lyster et al. (2021). We then estimated the median grain-size
214 (D_{50}) using size terms of the Wentworth (1922) classification (Fig. 3a,b). When converted to
215 numerical values, we assigned the middle value for each size term or, where grain-size
216 straddled two size terms, we used the boundary value, e.g., D_{50} of medium-grade sand = 0.375
217 mm and medium–coarse-grade sand = 0.5 mm (Wentworth, 1922). We repeated this for
218 multiple cross-sets within co-sets. Having measured thickness distributions within individual
219 cross-sets, we then measured a sample of maximum cross-set thicknesses (i.e., the maximum
220 distance between lower and upper bounding surfaces) of cross-sets at each locality ($n\sim 25-$
221 75). These cross-sets were all related, spanning multiple co-sets that were confined, where
222 possible, to a single channelized sandstone body.

223 For each individual cross-set, we calculated the mean cross-set thickness, h_{xs} , the maximum
224 thickness, and the CV of the internal thickness distribution ($CV(h_{xs})$) — a key parameter to test
225 whether the bedforms are preserved in steady-state or disequilibrium conditions. For each
226 sample of maximum cross-set thicknesses, we similarly calculated the mean maximum cross-
227 set thickness, h_p , and the CV of the entire sample ($CV(h_p)$), and we additionally analysed the
228 shape of each distribution.

229 We then propagated mean thicknesses of individually measured cross-sets (and their
230 respective grain-sizes) through a well-established quantitative framework (c.f. Ganti et al.,
231 (2019), Lyster et al., (2021); Supplementary Methods) to reconstruct bedform turnover
232 timescales — we can use these values to contextualise the implications of the flood and
233 hierarchy hypotheses. For instance, under the flood hypothesis we expect waning flow
234 durations to be shorter than turnover timescales, whereas under the hierarchy hypothesis we
235 expect bars to be migrating on timescales that approach bedform turnover timescales. We
236 reconstructed turnover timescales, T_t , i.e., the time taken to displace the volume of sediment
237 of the bedform (per unit width), following Martin and Jerolmack (2013) and Myrow et al.
238 (2018), as:

$$T_t = \frac{\lambda h_d \beta}{q_b}, \quad [\text{Eq. 1}]$$

239 where λ is bedform wavelength, which we estimated using the depth scaling relation of van
240 Rijn (1984), h_d is bedform (i.e., dune) height, $\beta \sim 0.55$ is the bedform shape factor and q_b is the
241 unit bedload flux, which we calculated following Mahon and McElroy (2018) (Supplementary
242 Methods). As the exact error margins of palaeohydraulic inversion methods are unknown, we
243 used a Monte Carlo uncertainty propagation method to estimate uncertainty, which yielded
244 10^6 values of T_t per cross-set (Supplementary Methods). From these estimates we extracted
245 median T_t , the 25–75 percentile range of T_t , and the 10–90 percentile range of T_t . For each
246 cross-set, we suggest that the 10–90 percentile range of T_t offers a plausible minimum and
247 maximum value for mean T_t , and that the 25–75 percentile range of T_t offers the bounds in
248 which the true value of mean T_t is most likely to occur.

249 Reconstruction of T_t requires a priori knowledge of the bedform preservation ratio (h_{xs}/h_d),
250 which itself is a function of whether bedforms were preserved in steady-state or
251 disequilibrium conditions. To evaluate a maximum T_t value, we used $h_{xs}/h_d = 0.3$, which
252 reflects steady-state preservation under low bedform climb angle. We then assessed the
253 sensitivity of T_t to h_{xs}/h_d by repeating the methodology outlined above for h_{xs}/h_d values from
254 0 to 1. In the absence of preserved formsets that reflect $h_{xs}/h_d \geq 1.0$ (Reesink et al., 2015),
255 enhanced bedform preservation is characterized by $0.3 < h_{xs}/h_d \leq 0.7$ (Supplementary
256 Information; Jerolmack and Mohrig (2005); Reesink et al. (2015); Ganti et al. (2020); Leary and
257 Ganti (2020)). For the sensitivity analyses, we used the h_{xs} and D_{50} of each measured cross-
258 set and calculated the overall mean h_{xs} and mean D_{50} for the Blackhawk Formation, Castlegate
259 Sandstone and Ferron Sandstone, respectively.

260 4. Results

261 4.1 Cross-set geometries

262 We present results aggregated at the formation scale, with no spatial or temporal reference
263 frame, as ancillary field observations suggest there is little variation between field sites (see

264 Supplementary Information and Lyster et al., (2021)). We measured >400 individual dune-
265 scale cross-sets of the Blackhawk Formation (n = 81), Castlegate Sandstone (n = 146) and
266 Ferron Sandstone (n = 190) (Fig. 4), with ~5–15 height measurements per cross-set, totalling
267 >3800 measurements. For each cross-set we recorded grain-size, which is reported in the
268 Supplementary Information, and we calculated the mean thickness and the maximum
269 thickness. Distributions of mean cross-set thicknesses are similar for the Blackhawk Formation
270 and Castlegate Sandstone (two-sample t-test; p = 0.067; test statistic = -1.838, degrees of
271 freedom = 225); distributions have median values of ~0.13–0.14 m and 10–90 percentile
272 ranges of 0.1–0.2 m. Distributions of maximum cross-set thicknesses for the Blackhawk
273 Formation and Castlegate Sandstone generally have medians of 0.17–0.18 m and 10–90
274 percentile ranges of 0.13–0.27 m (Fig. 4a,b). Whereas for the Ferron Sandstone, cross-sets
275 are larger with broader percentile ranges. The distribution of mean cross-set thicknesses has
276 a median of 0.15 m and a 10–90 percentile range of 0.08–0.25 m, and the distribution of
277 maximum cross-set thicknesses has a median of 0.22 m and a 10–90 percentile range of 0.12–
278 0.45 m (Fig. 4c).

279 We also measured maximum thicknesses of >3000 dune-scale cross-sets across the
280 Blackhawk Formation (801 measurements across 26 samples), Castlegate Sandstone (1015
281 measurements across 27 samples) and Ferron Sandstone (1257 measurements across 21
282 samples), with between 25–75 measurements per sample (Fig. 5). For each formation,
283 distributions of maximum thicknesses of cross-sets have median values of ~0.2 m (Fig. 5);
284 these values are consistent with maximum values extracted from individually measured cross-
285 sets (Fig. 4). For the Blackhawk Formation and Castlegate Sandstone, 90% of maximum cross-
286 set thicknesses are between ~0.15–0.3 m, and the upper 10% of maximum cross-set
287 thicknesses are markedly larger (≤ 0.5 – 0.6 m) (Fig. 5a,c). Meanwhile, for the Ferron
288 Sandstone, 90% of maximum cross-set thicknesses are between ~0.15–0.35 m and the upper
289 10% of maximum cross-set thicknesses are also markedly larger (≤ 0.7 m) (Fig. 5e). These
290 distributions of maximum cross-set thicknesses across all cross-set samples are generally
291 mirrored in individual cross-set samples (Fig. 5b,d,f), with median values of ~0.2 m, suggesting
292 they are not from a limited subset of locations. Most samples of maximum cross-set
293 thicknesses demonstrate positively-skewed, long-tailed distributions wherein relatively few
294 large cross-sets exist among abundant smaller cross-sets (Fig 5b,d,f). The kurtosis of
295 distributions varies for each formation, such that distributions in the Castlegate Sandstone
296 and Ferron Sandstone are more long-tailed than in the Blackhawk Formation (Fig 5b,d,f).

297 Our data show that CV values of cross-set thicknesses are significantly lower than the
298 expected steady-state values of 0.88 (Fig. 6). We found low CV of thicknesses within individual
299 cross-sets ($CV(h_{xs})$), as well as low CV of thicknesses for a sample of measured cross-sets
300 within related co-sets ($CV(h_p)$) (Fig. 6). In the Blackhawk Formation and Castlegate Sandstone,
301 median $CV(h_{xs})$ is 0.3 with a 25–75 percentile range of ~0.25–0.38, and maximum $CV(h_{xs})$
302 extends to 0.45–0.55 (Fig. 6a,b). The Ferron Sandstone $CV(h_{xs})$ values are also low (relative to
303 steady-state) but are higher than in the Blackhawk–Castlegate succession. For the Ferron

304 Sandstone, median $CV(h_{xs})$ is 0.4 with a broader 25–75 percentile range of ~ 0.3 – 0.5 , and
305 maximum $CV(h_{xs})$ extends to 0.6 – 0.75 (Fig. 6c). We found that none of the measured $CV(h_{xs})$
306 values were consistent with the proposed empirical range of 0.88 ± 0.30 for steady-state
307 preservation (Bridge, 1997) in the Blackhawk–Castlegate succession; however, 6% of the
308 measurements were within this range for the Ferron Sandstone. For $CV(h_p)$, recovered values
309 are even lower. In the Blackhawk Formation and Castlegate Sandstone median $CV(h_p)$ is 0.2,
310 with 25–75 percentile ranges of ~ 0.15 – 0.25 (Fig. 6a,b), and in the Ferron Sandstone median
311 $CV(h_p)$ is 0.3, with a 25–75 percentile range of ~ 0.25 – 0.35 (Fig. 6c).

312 **4.2 Maximum bedform turnover timescales**

313 We first present results for reconstructed T_t values for each formation using a bedform
314 preservation ratio of 0.3, and then explore the sensitivity of T_t to $h_{xs}/h_d > 0.3$ which is expected
315 for the preservation of bedforms under high angles of local bedform climb. The geometries
316 and grain-sizes of measured cross-sets imply that T_t values typically span 1–10 days, with a
317 median value of 2–4 days (Fig. 7). The overall distributions of T_t vary between the geologic
318 formations (Fig. 7). For the Castlegate Sandstone median T_t is 2.5–3 days, with a 10–90
319 percentile range of 1–7 days (Fig. 7a). For the Blackhawk Formation, values are marginally
320 higher with a median T_t of 3–3.5 days, and a 10–90 percentile range of 1.5–8 days (Fig. 7b).
321 While the Ferron Sandstone has a similar median T_t of 3–3.5 days, it has a much broader 10–
322 90 percentile range spanning < 1 –15 days (Fig. 7c).

323 We recovered 10^6 values of T_t for each cross-set using a Monte Carlo approach (see Methods
324 and Supplementary Methods) and the results described above present the cumulative
325 distribution function (CDF) of median T_t values for each cross-set (Fig. 7). We also computed
326 the CDFs for the 10th, 25th, 75th and 90th percentiles of T_t values of each cross-set to highlight
327 the plausible range of values that are consistent with field observations. These CDFs
328 demonstrate that, despite uncertainty in T_t of up to one order of magnitude, the majority of
329 possible T_t values are between 1 and 10 days (Fig. 7). These T_t values suggest that floods with
330 typical recessions > 10 days would have fully equilibrated bedforms, similar to observations in
331 relatively shallow modern rivers (Leary & Ganti, 2020). Further, the estimated maximum T_t of
332 2–4 days, with an overall span of 1–10 days (Fig. 7) for dune-scale cross-strata in the
333 Blackhawk–Castlegate succession and the Ferron sandstone are consistent with dune
334 migration in modern natural rivers (e.g., Hajek & Straub, 2017; Leary & Ganti, 2020).

335 **4.3 Sensitivity of bedform turnover timescales to bedform preservation ratio**

336 To assess the sensitivity of T_t to h_{xs}/h_d , we systematically varied h_{xs}/h_d for each formation from
337 0 to 1 (Fig. 8), where the former indicates no preservation and the latter implies complete
338 preservation of formsets. An increase in h_{xs}/h_d corresponds analytically with a decrease in T_t
339 (see Supplementary Methods). For example, increasing h_{xs}/h_d by a factor of 2, from 0.3 to 0.6,
340 reduces T_t by a factor of 5–6 (Fig. 8). Compared to results for $h_{xs}/h_d \sim 0.3$, the median T_t values
341 for the Castlegate Sandstone and the Blackhawk Formation are smaller by a factor of 5, with

342 median T_t of 0.7 days (~17 hours) and 1 day, respectively (Figs. 8a, b). For the Ferron
343 Sandstone, $h_{xs}/h_d=0.6$ reduces the median T_t by a factor of 6 to ~1 day, when compared to
344 $h_{xs}/h_d\sim 0.3$ (Fig. 8c). In all cases, extreme dune preservation with $h_{xs}/h_d=1$ yielded $T_t < 0.1$ days,
345 and extremely low values of $h_{xs}/h_d \ll 0.3$ yielded unrealistic T_t values as high as 10^5 days (Fig.
346 8). Experimental bedform preservation under steady and unsteady flows indicates that the
347 h_{xs}/h_d may likely span 0.3 and 0.7 (grey bars, Fig. 8; Supplementary Information) in the
348 absence of evidence for formset preservation (Leary & Ganti, 2020).

349 5. Discussion

350 From >400 individually measured dune-scale cross-sets ($n=5-15$ measurements per cross-set)
351 across the three geologic formations, our results indicated that estimated $CV(h_{xs})$ was always
352 lower than 0.88 and ranged from ~0.25–0.5 (Fig. 6). Across these formations, only 3% of the
353 estimated $CV(h_{xs})$ were consistent with the empirical range of 0.88 ± 0.30 expected for
354 bedform preservation under steady-state conditions (Bridge, 1997). Low $CV(h_{xs})$ is
355 inconsistent with steady-state preservation of bedforms and does not support generation of
356 cross-sets by random variability in scour depths through time (Paola & Borgman, 1991; Leclair
357 & Bridge, 2001; Leclair, 2002; Jerolmack & Mohrig, 2005). Instead, our observations provide
358 evidence for enhanced bedform preservation driven by localized increase in sedimentation
359 rates relative to the bedform migration rates (Jerolmack & Mohrig, 2005; Ganti et al., 2020;
360 Leary & Ganti, 2020), suggesting that river dune deposits of the Blackhawk Formation,
361 Castlegate Sandstone, and Ferron Sandstone are dominated by bedform disequilibrium
362 dynamics. Below we discuss the implications of these observations under the flood and
363 hierarchy hypotheses and delineate potential approaches to disentangle their relative roles
364 in ancient fluvial systems.

365 5.1 Implications of the flood hypothesis for bedform preservation

366 Using physical experiments, Leary and Ganti (2020) showed that, where bedform
367 disequilibrium dynamics are only controlled by formative flow variability, low $CV(h_{xs})$ indicates
368 a scenario in which the formative flow duration (T_f), i.e. the flood recession, is significantly
369 less than the bedform turnover timescale (T_t). Bedform disequilibrium dynamics associated
370 with formative flow variability typically manifest in rivers with flashy flood hydrographs, in
371 which river discharge is characterized by floods with a short flood recession period relative to
372 T_t (Leary & Ganti, 2020) — the rapid decline in water discharge following peak flood minimizes
373 bedform reworking and enhances bedform preservation (Leary & Ganti, 2020). Under the
374 flood hypothesis, the documented low $CV(h_{xs})$ is consistent with T_f values that are a factor of
375 10 smaller than T_t (assuming the ratio of T_f to T_t is ~0.1; c.f. Leary and Ganti (2020)). As the
376 maximum T_t values fall between 1–10 days for our field data, the estimated $CV(h_{xs})$ indicates
377 typical T_f values spanning 0.1–1 day (2.4–24 hours) for $h_{xs}/h_d\sim 0.3$. The range of plausible T_f
378 values consistent with experimentally observed bedform preservation ratios and field-

379 estimated $CV(h_{xs})$ is on the order of 0.1 days for all the geologic formations considered here
380 (Fig. 8).

381 Under the flood hypothesis, our field data unanimously indicate that flood recessions did not
382 exceed a few hours to a day for these Late Cretaceous fluvial systems. Given the typical shape
383 of flashy flood hydrographs, we also anticipate that total flood durations did not exceed a few
384 hours to a few days. Our estimated flood durations are plausible and consistent with recent
385 (decadal-scale) observations of modern rivers in sub-tropical and/or mid-latitude regions
386 (e.g., Serinaldi et al., 2018). Moreover, compilations of global flood data indicate that, for
387 flood durations on the order of hours to days, the main causes are: heavy rain, brief torrential
388 rain, tropical storms, and extra-tropical storms (Serinaldi et al., 2018). These flood durations,
389 and associated causes, are typical of perennial discharge regimes. While the Blackhawk
390 Formation, Castlegate Sandstone and Ferron Sandstone have not been explicitly studied in
391 terms of variable discharge facies models, existing facies analyses of these formations have
392 typically described sedimentary and architectural structures associated with perennial rivers
393 (see review by Plink-Björklund, 2015). These include abundant Froude subcritical structures
394 (i.e., cross-sets from which we collected data; Fig. 3) and well-developed macroforms (i.e.,
395 bars and accretion sets) (Cotter, 1971; Miall, 1994; Chidsey et al., 2004; Adams &
396 Bhattacharya, 2005; Hampson et al., 2013; Flood & Hampson, 2014; Chamberlin & Hajek,
397 2019).

398 Independent modelling and proxy studies of palaeoclimate in Late Cretaceous central Utah
399 suggest the region was subject to a sub-tropical/monsoonal climate with monsoonal
400 precipitation and frequent seasonal flooding in low-lying alluvial plains (e.g., Fricke et al.,
401 2010; Sewall & Fricke, 2013). However, floods caused by monsoonal rains typically have long
402 durations spanning ~5–25 days (Serinaldi et al., 2018). Additionally, an abundance of features
403 associated with monsoonal systems, e.g., in-channel mud layers, abundant soft-sediment
404 deformation, soft-sediment clast conglomerates (see review by Plink-Björklund, 2015), have
405 not been reported in the literature for these formations or observed at our field localities.
406 Given that our reconstructed flood durations and existing facies models indicate perennial
407 discharge regimes, the flood hypothesis indicates that these river dune deposits could record
408 bedform adjustment to flooding associated with storm events as opposed to sustained
409 monsoonal flooding.

410 **5.2 Implications of the hierarchy hypothesis for bedform preservation**

411 Under the alternative hierarchy hypothesis, enhanced bedform preservation is facilitated by
412 self-organization of fluvial systems into a series of hierarchical elements (Ganti et al., 2020),
413 where the nature of preservation of topography within a given hierarchical level is solely
414 controlled by the next level in the morphodynamic hierarchy. The presence of bars — the
415 higher-order hierarchical elements of dunes — will locally enhance preservation of river
416 dunes because the bars both provide accommodation for bedforms and increase bedform

417 climb angles (Reesink et al., 2015; Ganti et al., 2020). Cardenas et al. (2020) observed low
418 $CV(h_{xs})$ for dune-scale cross-strata on the stoss and lee slopes of point bar and free bar
419 deposits, when compared to dune-scale cross-strata in thalweg deposits of the Cretaceous
420 Cedar Mountain Formation, Utah, which is consistent with the hierarchy hypothesis for
421 bedform preservation. Numerical models indicate that observed low $CV(h_{xs})$ values are
422 associated with rapid sedimentation rates relative to bedform migration rates such that the
423 bedform climb angle is of the order of 10^{-2} to 10^{-1} (Jerolmack & Mohrig, 2005). Given that the
424 local angle of climb for bedforms is influenced by the relative rates of dune migration to bar
425 migration (Ganti et al., 2020), these results suggest low $CV(h_{xs})$ values measured in the field
426 are consistent with timescales of bar migration on the order of days to months.

427 The nature of stratigraphic architecture, particularly of barform deposits, is well-documented
428 for the Blackhawk Formation, Castlegate Sandstone and Ferron Sandstone (Cotter, 1971;
429 Miall, 1993, 1994; Chidsey et al., 2004; Adams & Bhattacharya, 2005; Hampson et al., 2013;
430 Flood & Hampson, 2014; Chamberlin & Hajek, 2019; Lyster et al., 2021). The Castlegate
431 Sandstone comprises amalgamated fluvial channel-belt deposits which, architecturally, are
432 dominated by barforms (e.g., mid-channel bars) (Miall, 1993, 1994; Chamberlin & Hajek,
433 2019). Therefore, dune-scale cross-sets that we measured in the Castlegate Sandstone likely
434 preserve dunes that were influenced by bar migration, and it is possible that low $CV(h_{xs})$
435 values observed in these cross-sets reflect bedform disequilibrium dynamics associated with
436 the hierarchy hypothesis, especially given that unit bar migration typical of braided rivers can
437 be comparable to dune migration rates (Strick et al., 2019). Conversely, fluvial strata of the
438 Blackhawk Formation and Ferron Sandstone comprise major channelized sandstone bodies
439 (Cotter, 1971; Chidsey et al., 2004; Adams & Bhattacharya, 2005; Hampson et al., 2013; Flood
440 & Hampson, 2014) which, while abundant in barforms (e.g., laterally accreted point bar
441 deposits; Fig. 2f), also likely preserve a much larger proportion of channel deposits that are
442 devoid of barform architecture and which may reflect thalweg deposits. Cardenas et al. (2020)
443 hypothesized that thalweg strata represent aggradation in channel beds during the final flood
444 event prior to channel avulsion. We therefore consider that enhanced bedform preservation
445 in thalweg deposits of the Blackhawk Formation and Ferron Sandstone is less likely to reflect
446 bedform preservation in the presence of rapid bar migration and, instead, is more likely to
447 reflect formative flow variability.

448 **5.3 Detangling flood versus hierarchy controls on bedform preservation**

449 While both the flood hypothesis and the hierarchy hypothesis explain the observed
450 dominance of enhanced bedform preservation, disentangling their relative roles in controlling
451 bedform preservation is currently non-trivial. We hypothesize that spatially contextualizing
452 the observed deposits may be critical for evaluating the controls on bedform preservation.
453 For example, it is likely that dunes preserved in channel-thalweg deposits of single-thread
454 rivers are not influenced by the presence of bars and, therefore, may reflect the formative
455 flood variability. This scenario may be similar to physical experiments that do not exhibit the

456 multiple morphodynamic hierarchical levels that typify natural rivers. We hypothesise that,
457 where low $CV(h_{xs})$ values are observed in dune-scale cross-sets associated with thalweg
458 deposits, we can use estimated bedform turnover timescales to constrain formative flow
459 durations. Similarly, field observations indicate that dunes preserved in the presence of bars
460 are likely to be better preserved than expected under steady-state conditions (Reesink et al.,
461 2015; Cardenas et al., 2020). In this scenario, $CV(h_{xs})$ may yield insight into the relative rates
462 at which bedforms and barforms migrated in ancient fluvial systems.

463 Together, single-thread river deposits may display a larger range of $CV(h_{xs})$ that reflects both
464 formative flow variability and the relative kinematic rates of evolution of successive
465 hierarchical levels in the morphodynamic hierarchy. In contrast, braided rivers are
466 characterized by relatively rapid migration of unit bars and free bars in the presence of river
467 dunes (e.g., Strick et al., 2019) and detangling the role of morphodynamic hierarchy and flood
468 variability may be more difficult. Our results are consistent with this expectation as we
469 observe a larger range of $CV(h_{xs})$ for single-thread river deposits of the Ferron Sandstone
470 compared to the predominantly braided river deposits of the Castlegate Sandstone (Fig. 6).
471 Nonetheless, this work provides a basis for further testing the roles of flow variability and
472 morphodynamic hierarchy on the preservation of bedform dynamics, including other causes
473 of non-uniform flow such as channel abandonment and backwater hydraulics (e.g., Wu et al.,
474 2020).

475 In terms of cross-set geometries, a promising avenue to decipher the dominant control on
476 bedform disequilibrium dynamics is to compare population statistics of related cross-sets,
477 measured in the field, with those from experimental observations. For instance, Leary and
478 Ganti (2020) showed that, in flashy flood hydrographs, the rapid decline of water discharge
479 associated with short waning-flow durations enhances preservation of relatively larger, peak-
480 flood equilibrated, dunes (Leary & Ganti, 2020). In this scenario, we expect maximum cross-
481 set thicknesses to have a positively skewed long-tailed distribution with large cross-sets
482 interspersed with relatively smaller cross-sets (Leary & Ganti, 2020). Whereas bedform
483 preservation in steady-state conditions, or under a broad flood hydrograph, will likely result
484 in maximum cross-set thicknesses that have a short-tailed distribution, with a much higher
485 frequency of smaller cross-sets, as longer waning-flow durations enable reworking of larger
486 dunes such that the preservation potential of peak-flood equilibrated dunes is low (Leclair,
487 2011; Leary & Ganti, 2020). Across our measured samples, distributions of maximum cross-
488 set thicknesses are consistent with bedform preservation under the flood hypothesis; most
489 samples have long-tailed, positively skewed distributions (Figs 5b,d,f). Based on these
490 considerations, we judge it plausible that fluvial stratigraphy in the Blackhawk Formation and
491 Ferron Sandstone may record bedform disequilibrium dynamics driven by formative flow
492 variability, associated with the magnitudes and timescales of individual discharge events on
493 the timescale of hours to days. Future experimental and modelling work should investigate
494 whether and how bedform preservation ratios and the statistical nature of preserved cross-
495 sets differs between systems in which bedform disequilibrium dynamics are driven by flashy

496 flood hydrographs versus coevolution of dunes and bars, respectively. We advocate that this
497 is the next step in determining the extent to which discharge variability can be quantitatively
498 reconstructed from stratigraphic observations.

499 Ultimately, despite sampling a variety of fluvial planform styles across large geographic
500 regions, our results indicate that measured dune-scale cross-sets do not demonstrate the
501 geometries expected for bedform preservation under steady-state conditions, which
502 routinely underpin palaeohydraulic investigations of ancient fluvial systems. This indicates
503 that application of bedform preservation ratios of ~ 0.3 to fluvial strata may result in
504 overestimation of true palaeoflow depths (c.f. Leclair & Bridge, 2001) and consequently
505 underestimate palaeoslopes. We argue that systematic measurements of cross-set
506 geometries and, where possible, bedform preservation ratios should be a routine tool to
507 facilitate and contextualize palaeohydraulic reconstructions, and to test for the presence of
508 bedform disequilibrium dynamics.

509 **6. Conclusions**

510 We made systematic measurements of dune-scale cross-set geometries and grain-sizes in
511 fluvial strata of three Late Cretaceous geologic formations in central Utah, USA: the
512 Blackhawk Formation, Castlegate Sandstone, and Ferron Sandstone. Across all three
513 formations, we documented unanimously low $CV(h_{xs})$ in preserved cross-set thicknesses of
514 0.25–0.5. These field observations are inconsistent with the steady-state bedform
515 preservation model that assumes cross-sets are generated by random variability in scour
516 depth with time (Paola & Borgman, 1991; Leclair & Bridge, 2001). Instead, our observations
517 add to the growing recognition that bedform preservation is dominated by disequilibrium
518 dynamics (Reesink et al., 2015; Ganti et al., 2020; Leary & Ganti, 2020), resulting in higher
519 bedform preservation ratios and the deposition of cross-sets which preserve a relatively
520 narrow distribution of thicknesses ($CV(h_{xs}) < 0.88$).

521 We considered two independent hypotheses that lead to enhanced bedform preservation in
522 disequilibrium conditions. Under the flood hypothesis, our data indicate that the flood
523 durations that typify these deposits likely ranged from hours to days, which are reflective of
524 heavy rain and tropical storms in these ancient fluvial landscapes. Under the hierarchy
525 hypothesis, the observed low $CV(h_{xs})$ is consistent with bedform deposits preserved with
526 rapidly evolving bars whose timescale of migration likely spans days to months. Detangling
527 the flood versus hierarchy controls on bedform preservation may be possible through the
528 spatial contextualization of preserved deposits of single-thread rivers, with flow variability
529 potentially the dominant control on the nature of bedform preservation in channel-thalweg
530 deposits, such as those observed in the Ferron Sandstone and Blackhawk Formation.
531 However, detangling these relative controls may be difficult in the deposits of braided rivers,
532 such as the Castlegate Sandstone, that are characterized by migration of unit bars and braid
533 bars that can lead to the enhanced bedform preservation.

534 Where low $CV(h_{xs})$ reflects enhanced bedform preservation associated with formative flow
535 variability, the approaches presented in this paper have significant implications for
536 investigating discharge variability in the geologic past, particularly the magnitudes, transport
537 capacities, and durations of individual flood events generated during short-period climatic
538 perturbations. Meanwhile, where low $CV(h_{xs})$ reflects enhanced bedform preservation
539 associated with the presence of a morphodynamic hierarchy, these results have implications
540 for evaluating the nature of interactions between dunes, bars, channel migration and channel
541 avulsion in palaeo-channel networks. We advocate that quantifying cross-set geometries
542 should become a standard approach in future studies to improve and contextualize
543 palaeohydrological reconstructions from ancient fluvial deposits.

544 **Acknowledgements**

545 This research was primarily funded by a Natural Environment Research Council (NERC)
546 Science and Solutions for a Changing Planet Doctoral Training Partnership (DTP) grant to SJL,
547 with additional funding by The Geological Society of London and The British Sedimentological
548 Research Group to SJL. We thank George Hedley and Bailey Lathrop for support with field
549 data collection, and we thank the Safiya Alpheus for useful discussions. We would also like to
550 thank Luca Colombera and one anonymous reviewer for their constructive reviews, which
551 have greatly improved this manuscript.

552 **Data Availability**

553 Field data available in the Supplementary Information.

554 **References**

- 555 Adams, M. M., & Bhattacharya, J. P. (2005). No change in fluvial style across a sequence boundary,
556 Cretaceous Blackhawk and Castlegate formations of central Utah, U.S.A. *Journal of*
557 *Sedimentary Research*, 75(6), 1038-1051. doi:10.2110/jsr.2005.080
- 558 Allen, J. R. L. (1982). *Sedimentary Structures; Their Character and Physical Basis. Volume I* (Vol. 30).
559 Amsterdam: Elsevier.
- 560 Best, J. (2005). The fluid dynamics of river dunes: A review and some future research directions.
561 *Journal of Geophysical Research: Earth Surface*, 110(F4). doi:10.1029/2004JF000218
- 562 Bradley, R. W., & Venditti, J. G. (2017). Reevaluating dune scaling relations. *Earth-Science Reviews*,
563 165, 356-376. doi:10.1016/j.earscirev.2016.11.004
- 564 Bridge, J. S. (1997). Thickness of sets of cross strata and planar strata as a function of formative bed-
565 wave geometry and migration, and aggradation rate. *Geology*, 25(11), 971-974.
566 doi:10.1130/0091-7613(1997)025<0971:TOSOCS>2.3.CO;2
- 567 Cardenas, B. T., Mohrig, D., Goudge, T. A., Hughes, C. M., Levy, J. S., Swanson, T., Mason, J., & Zhao,
568 F. (2020). The anatomy of exhumed river-channel belts: Bedform to belt-scale river
569 kinematics of the Ruby Ranch Member, Cretaceous Cedar Mountain Formation, Utah, USA.
570 *Sedimentology*, 67(7), 3655-3682. doi:10.1111/sed.12765
- 571 Carling, P. A. (1999). Subaqueous gravel dunes. *Journal of Sedimentary Research*, 69(3), 534-545.
572 doi:10.2110/jsr.69.534

573 Chamberlin, E. P., & Hajek, E. A. (2019). Using bar preservation to constrain reworking in channel-
574 dominated fluvial stratigraphy. *Geology*, 47(6), 531-534. doi:10.1130/G46046.1

575 Chidsey, T. C., Adams, R. D., & Morris, T. H. (2004). *Regional to Wellbore Analog for Fluvial-Deltaic*
576 *Reservoir Modeling: The Ferron Sandstone of Utah* (Vol. 50).

577 Colombera, L., Arévalo, O. J., & Mountney, N. P. (2017). Fluvial-system response to climate change:
578 The Paleocene-Eocene Trepmp Group, Pyrenees, Spain. *Global and Planetary Change*, 157, 1-
579 17. doi:10.1016/j.gloplacha.2017.08.011

580 Cotter, E. (1971). Paleoflow characteristics of a late Cretaceous river in Utah from analysis of
581 sedimentary structures in the Ferron sandstone. *Journal of Sedimentary Research*, 41, 129-
582 138. doi:10.1306/74D72202-2B21-11D7-8648000102C1865D

583 Edgar, L. A., Gupta, S., Rubin, D. M., Lewis, K. W., Kocurek, G. A., Anderson, R. B., Bell III, J. F.,
584 Dromart, G., Edgett, K. S., Grotzinger, J. P., Hardgrove, C., Kah, L. C., Leveille, R., Malin, M. C.,
585 Mangold, N., Milliken, R. E., Minitti, M., Palucis, M., Rice, M., Rowland, S. K., Schieber, J.,
586 Stack, K. M., Sumner, D. Y., Wiens, R. C., Williams, R. M. E., & Williams, A. J. (2018). Shaler:
587 in situ analysis of a fluvial sedimentary deposit on Mars. *Sedimentology*, 65(1), 96-122.
588 doi:10.1111/sed.12370

589 Fielding, C. R., Alexander, J., & Allen, J. P. (2018). The role of discharge variability in the formation
590 and preservation of alluvial sediment bodies. *Sedimentary Geology*, 365, 1-20.
591 doi:10.1016/j.sedgeo.2017.12.022

592 Flood, Y. S., & Hampson, G. J. (2014). Facies and architectural analysis to interpret avulsion style and
593 variability: Upper Cretaceous Blackhawk Formation, Wasatch Plateau, central Utah, U.S.A.
594 *Journal of Sedimentary Research*, 84(9), 743-762. doi:10.2110/jsr.2014.59

595 Foreman, B. Z., Heller, P. L., & Clementz, M. T. (2012). Fluvial response to abrupt global warming at
596 the Palaeocene/Eocene boundary. *Nature*, 491, 92-95. doi:10.1038/nature11513

597 Fricke, H. C., Foreman, B. Z., & Sewall, J. O. (2010). Integrated climate model-oxygen isotope
598 evidence for a North American monsoon during the Late Cretaceous. *Earth and Planetary*
599 *Science Letters*, 289(1-2), 11-21. doi:10.1016/j.epsl.2009.10.018

600 Ganti, V., Hajek, E. A., Leary, K., Straub, K. M., & Paola, C. (2020). Morphodynamic hierarchy and the
601 fabric of the sedimentary record. *Geophysical Research Letters*, 47(14), e2020GL087921.
602 doi:10.1029/2020GL087921

603 Ganti, V., Paola, C., & Fofoula-Georgiou, E. (2013). Kinematic controls on the geometry of the
604 preserved cross sets. *Journal of Geophysical Research: Earth Surface*, 118(3), 1296-1307.
605 doi:10.1002/jgrf.20094

606 Ganti, V., Whittaker, A., Lamb, M. P., & Fischer, W. W. (2019). Low-gradient, single-threaded rivers
607 prior to greening of the continents. *Proceedings of the National Academy of Sciences*, 116(4),
608 11652-11657. doi:10.1073/pnas.1901642116

609 Gardner, M. H., Cross, T. A., & Levorsen, M. (2004). Stacking Patterns, Sediment Volume Partitioning,
610 and Facies Differentiation in Shallow-Marine and Coastal-Plain Strata of the Cretaceous
611 Ferron Sandstone, Utah. In T. C. Chidsey, Jr., R. D. Adams, & T. H. Morris (Eds.), *Regional to*
612 *Wellbore Analog for Fluvial-Deltaic Reservoir Modeling: The Ferron Sandstone of Utah* (Vol.
613 50, pp. 0): American Association of Petroleum Geologists. doi:10.1306/St50983

614 Garrison, J. R., Jr., & Bergh, T. C. V. v. d. (2004). High-Resolution Depositional Sequence Stratigraphy
615 of the Upper Ferron Sandstone Last Chance Delta: An Application of Coal-Zone Stratigraphy.
616 In T. C. Chidsey, Jr., R. D. Adams, & T. H. Morris (Eds.), *Regional to Wellbore Analog for*

617 Fluvial-Deltaic Reservoir Modeling: The Ferron Sandstone of Utah (Vol. 50, pp. 0): American
618 Association of Petroleum Geologists. doi:10.1306/St50983

619 Ghinassi, M., Moody, J., & Martin, D. (2018). Influence of extreme and annual floods on point-bar
620 sedimentation: Inferences from Powder River, Montana, USA. *GSA Bulletin*, 131(1-2), 71-83.
621 doi:10.1130/B31990.1

622 Hajek, E. A., & Heller, P. L. (2012). Flow-depth scaling in alluvial architecture and nonmarine
623 sequence stratigraphy: Example from the Castlegate Sandstone, central Utah, U.S.A. *Journal*
624 *of Sedimentary Research*, 82(2), 121-130. doi:10.2110/jsr.2012.8

625 Hajek, E. A., & Straub, K. M. (2017). Autogenic sedimentation in clastic stratigraphy. *Annual Review*
626 *of Earth and Planetary Sciences*, 45(1), 681-709. doi:10.1146/annurev-earth-063016-015935

627 Hampson, G. J., Jewell, T. O., Irfan, N., Gani, M. R., & Bracken, B. (2013). Modest change in fluvial
628 style with varying accommodation in regressive alluvial-to-coastal-plain wedge: Upper
629 Cretaceous Blackhawk Formation, Wasatch Plateau, central Utah, U.S.A. *Journal of*
630 *Sedimentary Research*, 83(2), 145-169. doi:10.2110/jsr.2013.8

631 Herbert, C. M., Alexander, J., Amos, K. J., & Fielding, C. R. (2020). Unit bar architecture in a highly-
632 variable fluvial discharge regime: Examples from the Burdekin River, Australia.
633 *Sedimentology*, 67(1), 576-605. doi:10.1111/sed.12655

634 Holbrook, J., & Wanas, H. (2014). A fulcrum approach to assessing source-to-sink mass balance using
635 channel paleohydrologic parameters derivable from common fluvial data sets with an
636 example from the Cretaceous of Egypt. *Journal of Sedimentary Research*, 84(5), 349-372.
637 doi:10.2110/jsr.2014.29

638 Jerolmack, D. J., & Mohrig, D. (2005). Frozen dynamics of migrating bedforms. *Geology*, 33(1), 57-60.
639 doi:10.1130/G20897.1

640 Kauffman, E. G., & Caldwell, W. (1993). The Western Interior Basin in space and time. In E. G.
641 Kauffman & W. Caldwell (Eds.), *Evolution of the Western Interior Basin: Geological*
642 *Association of Canada, Special Paper 39* (pp. 1-30).

643 Leary, K. C. P., & Ganti, V. (2020). Preserved fluvial cross strata record bedform disequilibrium
644 dynamics. *Geophysical Research Letters*, 47(2), e2019GL085910. doi:10.1029/2019GL085910

645 Leclair, S. F. (2002). Preservation of cross-strata due to the migration of subaqueous dunes: an
646 experimental investigation. *Sedimentology*, 49(6), 1157-1180. doi:10.1046/j.1365-
647 3091.2002.00482.x

648 Leclair, S. F. (2011). Interpreting Fluvial Hydromorphology from the Rock Record: Large-River Peak
649 Flows Leave No Clear Signature. In S. K. Davidson, S. Leleu, & C. P. North (Eds.), *From River to*
650 *Rock Record: The preservation of fluvial sediments and their subsequent interpretation* (Vol.
651 97, pp. 0): SEPM Society for Sedimentary Geology. doi:10.2110/sepm.097.113

652 Leclair, S. F., & Bridge, J. S. (2001). Quantitative interpretation of sedimentary structures formed by
653 river dunes. *Journal of Sedimentary Research*, 71(5), 713-716. doi:10.1130/S0037-
654 1713/2001/0005-0000

655 Lynds, R., & Hajek, E. (2006). Conceptual model for predicting mudstone dimensions in sandy
656 braided-river reservoirs. *AAPG Bulletin*, 90 (8), 1273-1288. doi:10.1306/03080605051

657 Lyster, S. J., Whittaker, A. C., Hampson, G. J., Hajek, E. A., Allison, P. A., & Lathrop, B. A. (2021).
658 Reconstructing the morphologies and hydrodynamics of ancient rivers from source to sink:
659 Cretaceous Western Interior Basin, Utah, USA. *Sedimentology*. doi:10.1111/sed.12877

660 Mahon, R. C., & McElroy, B. (2018). Indirect estimation of bedload flux from modern sand-bed rivers
661 and ancient fluvial strata. *Geology*, 46(7), 579-582. doi:10.1130/G40161.1

662 Martin, R. L., & Jerolmack, D. J. (2013). Origin of hysteresis in bed form response to unsteady flows.
663 *Water Resources Research*, 49(3), 1314-1333. doi:10.1002/wrcr.20093

664 McLaurin, B. T., & Steel, R. J. (2007). Architecture and origin of an amalgamated fluvial sheet sand,
665 lower Castlegate Formation, Book Cliffs, Utah. *Sedimentary Geology*, 197(3), 291-311.
666 doi:10.1016/j.sedgeo.2006.10.005

667 Miall, A. D. (1993). The architecture of fluvial-deltaic sequences in the Upper Mesaverde Group
668 (Upper Cretaceous), Book Cliffs, Utah. In J. L. Best & C. S. Bristow (Eds.), Braided Rivers (Vol.
669 75, 305-332): *Geological Society, London, Special Publications*.
670 doi:10.1144/GSL.SP.1993.075.01.19

671 Miall, A. D. (1994). Reconstructing fluvial macroform architecture from two-dimensional outcrops;
672 examples from the Castlegate Sandstone, Book Cliffs, Utah. *Journal of Sedimentary Research*,
673 64(2b), 146-158. doi:10.1306/D4267F78-2B26-11D7-8648000102C1865D

674 Myrow, P. M., Jerolmack, D. J., & Perron, J. T. (2018). Bedform disequilibrium. *Journal of*
675 *Sedimentary Research*, 88(9), 1096-1113. doi:10.2110/jsr.2018.55

676 Paola, C., & Borgman, L. (1991). Reconstructing random topography from preserved stratification.
677 *Sedimentology*, 38(4), 553-565. doi:10.1111/j.1365-3091.1991.tb01008.x

678 Pettit, B. S., Blum, M., Pecha, M., McLean, N., Bartschi, N. C., & Saylor, J. E. (2019). Detrital-zircon U-
679 Pb paleodrainage reconstruction and geochronology of the Campanian Blackhawk-
680 Castlegate succession, Wasatch Plateau and Book Cliffs, Utah, U.S.A. *Journal of Sedimentary*
681 *Research*, 89(4), 273-292. doi:10.2110/jsr.2019.18

682 Plink-Björklund, P. (2015). Morphodynamics of rivers strongly affected by monsoon precipitation:
683 Review of depositional style and forcing factors. *Sedimentary Geology*, 323, 110-147.
684 doi:10.1016/j.sedgeo.2015.04.004

685 Reesink, A. J. H., Van den Berg, J. H., Parsons, D. R., Amsler, M. L., Best, J. L., Hardy, R. J., Orfeo, O., &
686 Szupiany, R. N. (2015). Extremes in dune preservation: Controls on the completeness of
687 fluvial deposits. *Earth-Science Reviews*, 150, 652-665. doi:10.1016/j.earscirev.2015.09.008

688 Romans, B. W., Castellort, S., Covault, J. A., Fildani, A., & Walsh, J. P. (2016). Environmental signal
689 propagation in sedimentary systems across timescales. *Earth-Science Reviews*, 153, 7-29.
690 doi:10.1016/j.earscirev.2015.07.012

691 Serinaldi, F., Loecker, F., Kilsby, C. G., & Bast, H. (2018). Flood propagation and duration in large river
692 basins: a data-driven analysis for reinsurance purposes. *Natural Hazards*, 94(1), 71-92.
693 doi:10.1007/s11069-018-3374-0

694 Sewall, J. O., & Fricke, H. C. (2013). Andean-scale highlands in the Late Cretaceous Cordillera of the
695 North American western margin. *Earth and Planetary Science Letters*, 362, 88-98.
696 doi:10.1016/j.epsl.2012.12.002

697 Straub, K. M., Duller, R. A., Foreman, B. Z., & Hajek, E. A. (2020). Buffered, incomplete, and
698 shredded: The challenges of reading an imperfect stratigraphic record. *Journal of*
699 *Geophysical Research: Earth Surface*, 125(3), e2019JF005079. doi:10.1029/2019JF005079

700 Strick, R. J. P., Ashworth, P. J., Sambrook Smith, G. H., Nicholas, A. P., Best, J. L., Lane, S. N., Parsons,
701 D. R., Simpson, C. J., Unsworth, C. A., & Dale, J. (2019). Quantification of bedform dynamics
702 and bedload sediment flux in sandy braided rivers from airborne and satellite imagery. *Earth*
703 *Surface Processes and Landforms*, 44(4), 953-972. doi:10.1002/esp.4558

704 Szwarc, T. S., Johnson, C. L., Stright, L. E., & McFarlane, C. M. (2015). Interactions between axial and
705 transverse drainage systems in the Late Cretaceous Cordilleran foreland basin: Evidence

706 from detrital zircons in the Straight Cliffs Formation, southern Utah, USA. *GSA Bulletin*,
707 127(3-4), 372-392. doi:10.1130/B31039.1

708 Ten Brinke, W. B. M., Wilbers, A. W. E., & Wesseling, C. (1999). Dune Growth, Decay and Migration
709 Rates during a Large-Magnitude Flood at a Sand and Mixed Sand–Gravel Bed in the Dutch
710 Rhine River System. In N. D. Smith & J. Rogers (Eds.), *Fluvial Sedimentology VI* (15-32).
711 doi:10.1002/9781444304213.ch2

712 Trampush, S. M., Huzurbazar, S., & McElroy, B. (2014). Empirical assessment of theory for bankfull
713 characteristics of alluvial channels. *Water Resources Research*, 50(12), 9211-9220.
714 doi:10.1002/2014WR015597

715 van Rijn, L. C. (1984). Sediment transport III: bedforms and alluvial roughness. *Journal of Hydraulic*
716 *Engineering*, 110(12), 1733-1754. doi:10.1061/(ASCE)0733-9429(1984)110:12(1733)

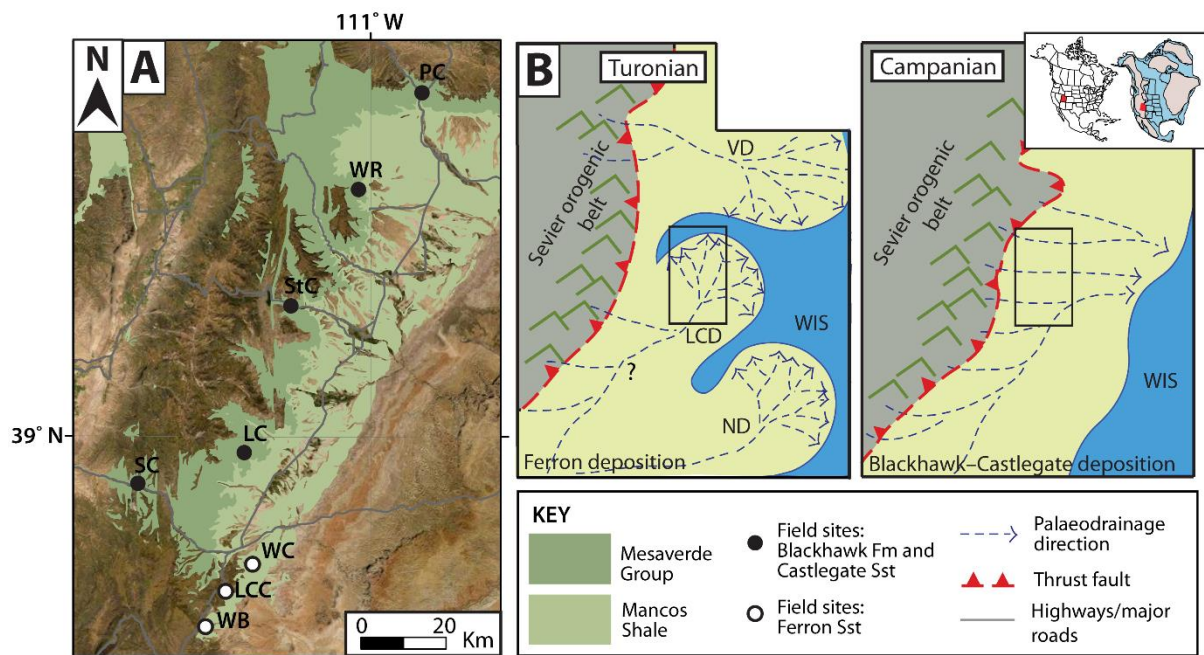
717 Wang, R., Colombera, L., & Mountney, N. P. (2020). Palaeohydrological characteristics and
718 palaeogeographic reconstructions of incised-valley-fill systems: Insights from the Namurian
719 successions of the United Kingdom and Ireland. *Sedimentology*, 67(7), 3844-3873.
720 doi:10.1111/sed.12773

721 Wentworth, C. K. (1922). A scale of grade and class terms for clastic sediments. *The Journal of*
722 *Geology*, 30(5), 377-392. doi:10.1086/622910

723 Wu, C., Nittrouer, J. A., Swanson, T., Ma, H., Barefoot, E., Best, J., & Allison, M. (2020). Dune-scale
724 cross-strata across the fluvial-deltaic backwater regime: Preservation potential of an
725 autogenic stratigraphic signature. *Geology*, 48(12), 1144-1148. doi:10.1130/G47601.1

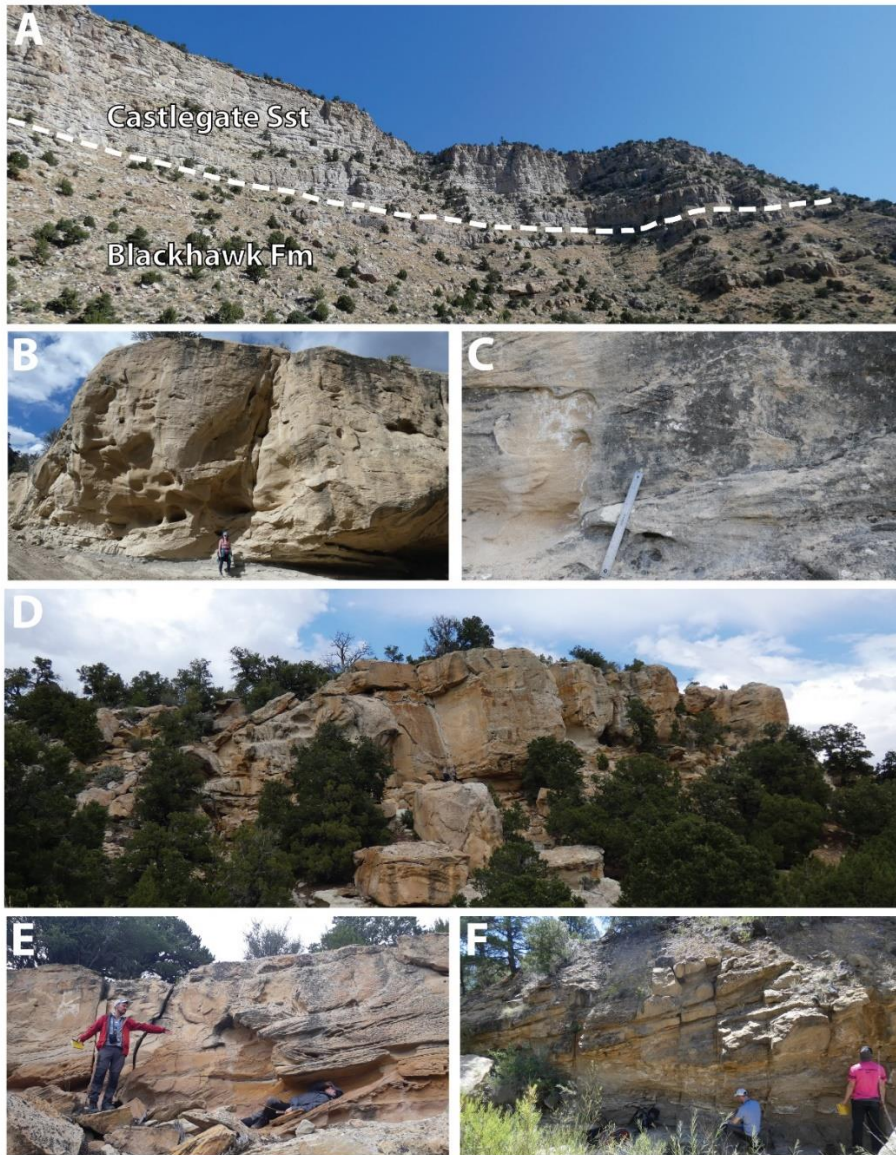
726 Wysocki, N., & Hajek, E. A. (2021). Mud in sandy riverbed deposits as a proxy for ancient fine-
727 sediment supply. *Geology*. doi:10.1130/G48251.1

728



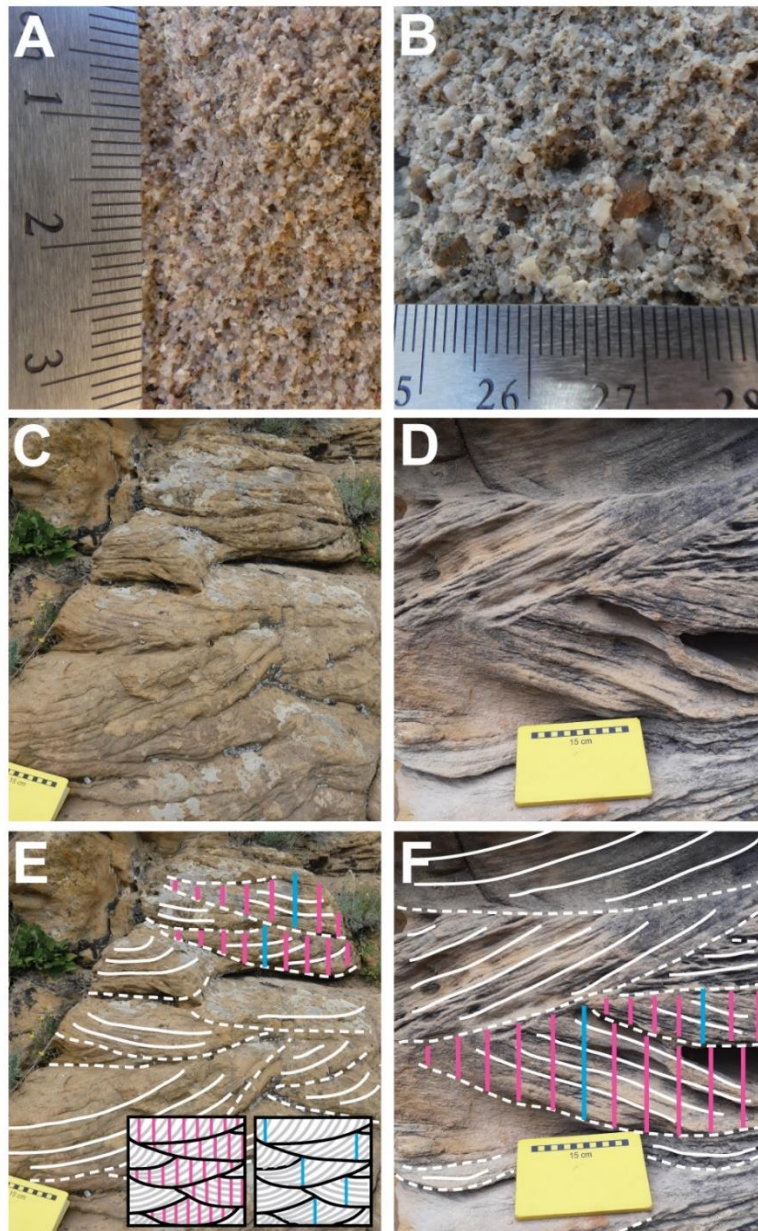
730

731 **Figure 1:** Study area. A) Field areas in central Utah, U.S.A., which include Last Chance Creek
 732 (LCC), Link Canyon (LC), Price Canyon (PC), Salina Canyon (SC), Straight Canyon (StC), Wattis
 733 Road (WR), Willow Basin (WB) and Willow Creek (WC). LC, PC, SC, StC and WR are field sites
 734 from which we obtained data for the Blackhawk Formation and Castlegate Sandstone
 735 (Mesaverde Group; black-filled circles). LCC, WB and WC are field sites from which we
 736 obtained data for the Ferron Sandstone (Mancos Shale; white-filled circles). B) A conceptual
 737 diagram of Utah palaeogeography and palaeodrainage in both the Turonian (left) and
 738 Campanian (right). Likely palaeodrainage configurations (and delta progradation)
 739 are indicated by dashed blue lines with arrows. The black outlined box in the centre of each
 740 palaeogeography indicates the study area (i.e., the approximate position and extent of A).
 741 The location of Utah relative to the modern North American continent (left) and the Late
 742 Cretaceous North American continent (right) is shown in the inset figure — Utah is highlighted
 743 as a red box. LCD = Last Chance delta; ND = Notom delta; VD = Vernal delta; WIS = Western
 744 Interior Seaway. Figure adapted from Lyster et al. (2021). [2 column figure]



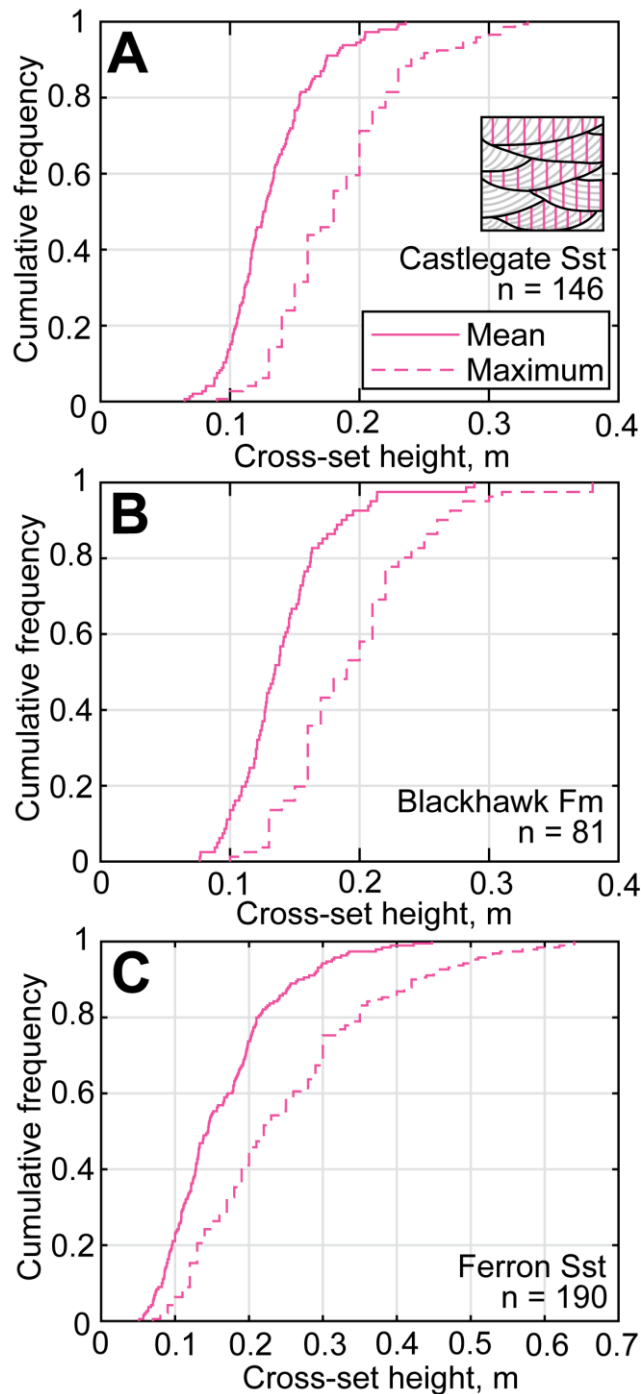
745

746 **Figure 2:** An overview of Upper Cretaceous fluvial strata from which we collected field data
 747 in central Utah, USA. A) Example of typical exposure of the Blackhawk Formation and
 748 Castlegate Sandstone (at Salina Canyon; SC; Fig. 1) which crops out in canyons along the
 749 eastern Wasatch front. Dashed white line indicates the lithostratigraphic boundary between
 750 the Blackhawk Formation and Castlegate Sandstone. Thickness of the Castlegate Sandstone
 751 is *ca* 85 m. B) Example of a major channelized fluvial sandstone body of the Blackhawk
 752 Formation at Link Canyon (LC; Fig. 1). C) Crude cross-stratification of amalgamated fluvial
 753 deposits of the Castlegate Sandstone at Price Canyon (PC; Fig. 1). D) Example of a major
 754 channelized sandstone body of the Ferron Sandstone at Last Chance Creek (LCC; Fig. 1).
 755 Persons for scale in centre of image. Thickness of channelized sandstone body in centre of
 756 image is *ca* 12 m. E) Cross-stratified fluvial strata of the Ferron Sandstone at LCC (with some
 757 soft-sediment deformation apparent). F) Laterally accreted point bar deposits of the Ferron
 758 Sandstone at LCC. [2 column figure]



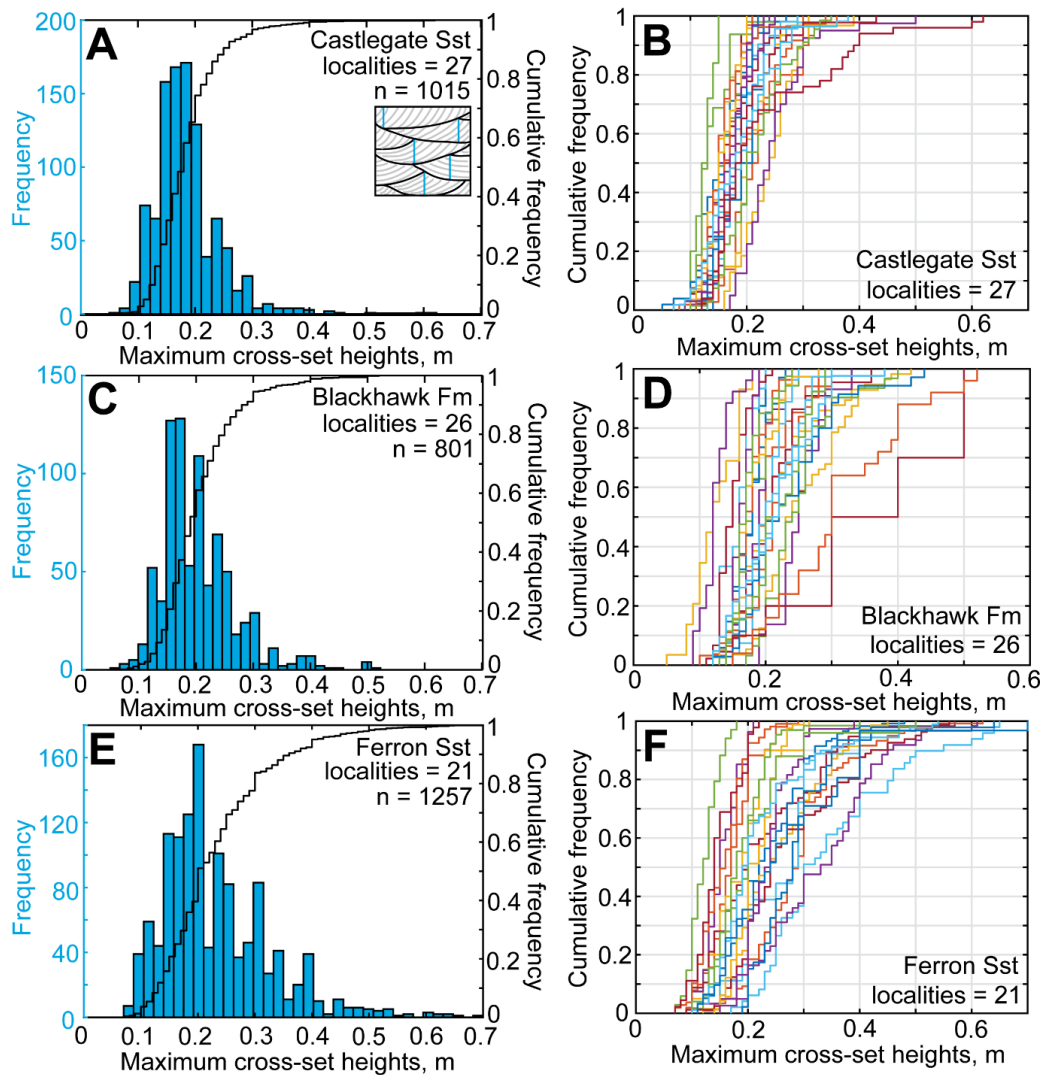
759

760 **Figure 3:** Field methods. A,B) For each measured cross-set, grain-size was assigned using the
 761 Wentworth (1922) classification. C,D) Examples of cross-sets from which distributions of
 762 cross-set heights were measured. E,F) Interpreted versions of the images in C,D. Dashed white
 763 lines indicate bounding surfaces between cross-sets and solid white lines indicate individual
 764 foresets within cross-sets. To exemplify how cross-sets were measured, pink vertical lines
 765 indicate the regular spacing within individual cross-sets at which heights were measured, and
 766 blue vertical lines indicate where maximum cross-set heights would have been measured for
 767 a population of cross-sets within co-sets at each locality. Insets in E are schematic
 768 representations of these two methods of data collection from cross-sets using pink and blue
 769 lines, respectively. Figure adapted from Lyster et al. (2021). [1 or 1.5 column figure]



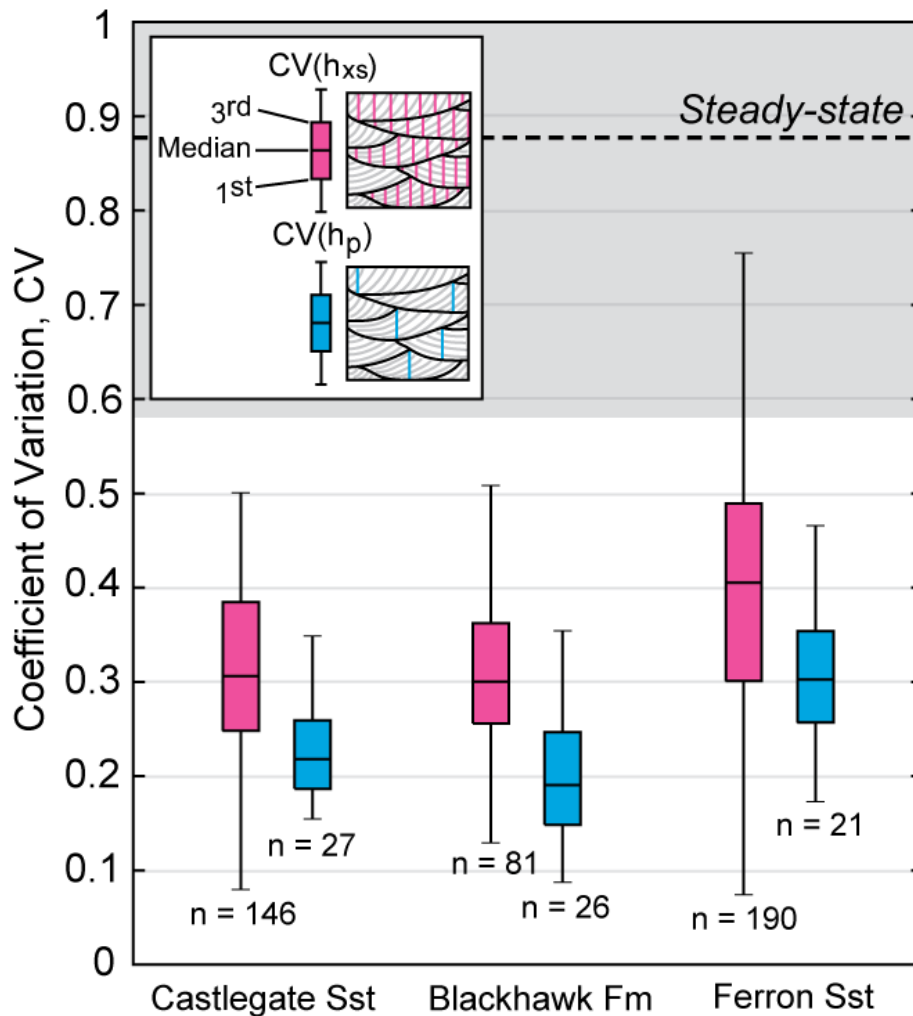
770

771 **Figure 4:** The cumulative frequency of the mean, median and maximum cross-set thickness
 772 for (A) the Castlegate Sandstone, (B) the Blackhawk Formation, and (C) the Ferron Sandstone.
 773 The solid pink line indicates the measured mean and the dashed pink line indicates the
 774 measured maximum. n indicates the number of cross-sets in which height distributions were
 775 measured, and therefore the number of cross-sets from which a mean and maximum were
 776 subsequently extracted. The inset in A is a schematic representation of how height
 777 distributions were measured within each cross-set. [1 column figure]



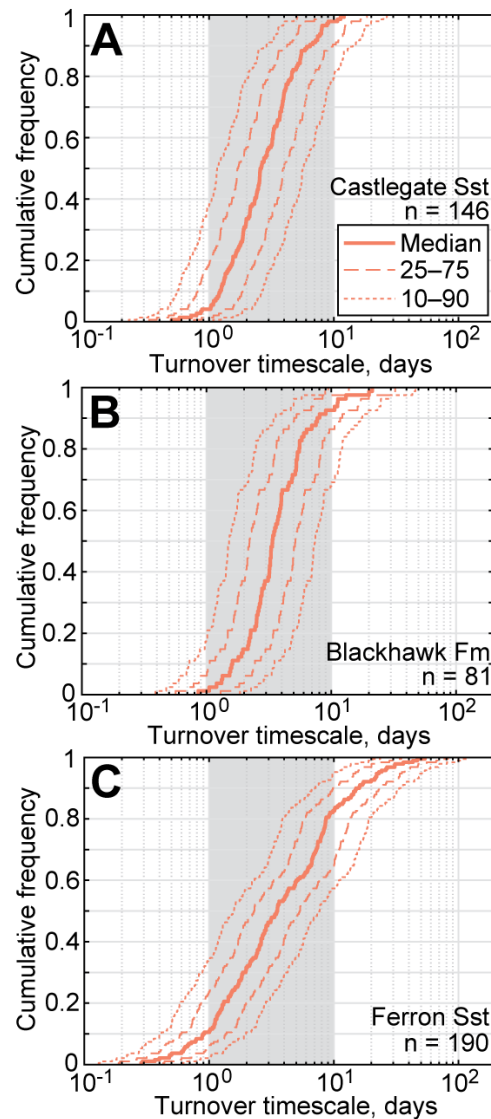
778

779 **Figure 5:** A) The frequency (left y axis; blue) and cumulative frequency (right y axis; black) of
 780 maximum cross-set heights measured across the Castlegate Sandstone. n indicates the total
 781 number of cross-sets measured for the entire formation, and the number of localities refers
 782 to the field sites across which these measurements were made. Measurements at each
 783 locality were for a population of related cross-sets within cosets, and typically comprised ~25–
 784 75 measurements. B) The cumulative frequency of maximum cross-set heights for each
 785 locality within the Castlegate Sandstone. C) The frequency and cumulative frequency of
 786 maximum cross-set heights measured across the Blackhawk Formation. D) The cumulative
 787 frequency of maximum cross-set heights for each locality within the Blackhawk Formation. E)
 788 The frequency and cumulative frequency of maximum cross-set heights measured across the
 789 Ferron Sandstone. F) The cumulative frequency of maximum cross-set heights for each
 790 locality within the Ferron Sandstone. The inset in A is a schematic representation of how
 791 maximum heights were measured across populations of cross-sets. [1.5 or 2 column figure]



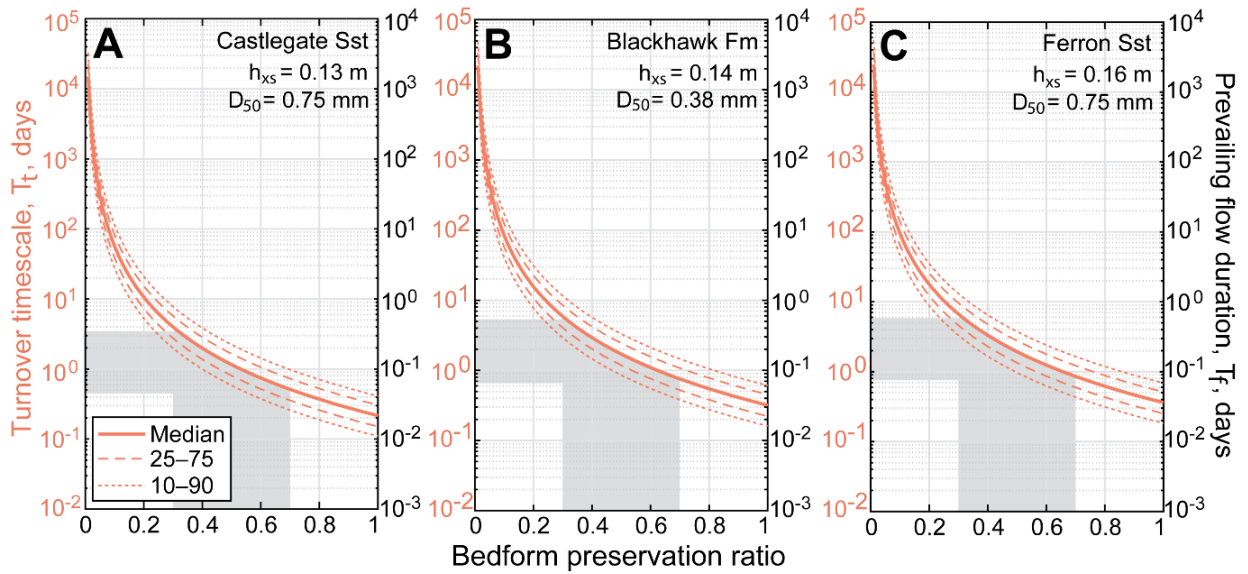
792

793 **Figure 6:** The coefficient of variation, CV , of cross-set heights measured in the Castlegate
 794 Sandstone, Blackhawk Formation, and Ferron Sandstone. Pink boxes indicate CV s of height
 795 distributions within individually measured cross-sets ($CV(h_{xs})$), with n indicating the number of
 796 individually measured cross-sets. The blue boxes indicate CV s of height distributions across a
 797 population of (related) cross-sets ($CV(h_p)$), with n indicating the number of field localities at
 798 which a population of cross-set heights was measured. At each locality, the population of
 799 measured cross-sets typically included ~ 25 – 75 cross-sets. Insets within the key demonstrate,
 800 schematically, how heights would have been measured for both $CV(h_{xs})$ and $CV(h_p)$
 801 respectively (see Methods). The central mark of each box indicates the median estimate, and
 802 the bottom and top edges of each box indicate the 1st and 3rd quartiles (or 25th and 75th
 803 percentiles), respectively. The whiskers extend to the most extreme values of CV that are not
 804 considered to be outliers. The dashed black line indicates the theoretical steady-state CV of
 805 0.88, following Paola and Borgman (1991), and the grey shaded region indicates the empirical
 806 steady-state CV of 0.88 ± 0.30 , following Bridge (1997). [1.5 column figure]



807

808 **Figure 7:** The cumulative frequency of estimated turnover timescales, T_t , calculated for (A)
 809 the Castlegate Sandstone, (B) the Blackhawk Formation, and (C) the Ferron Sandstone (see
 810 Supplementary Methods). T_t was calculated for each cross-set from which a cross-set height
 811 distribution was measured, using the mean height and the measured grain-size (Fig. 3; see
 812 Methods). n indicates the number of T_t values that were calculated (equal to the number of
 813 measured cross-set height distributions). The solid orange line indicates the median T_t
 814 reconstructed for each cross-set, the dashed orange lines indicate the 25th–75th percentile
 815 range of T_t values reconstructed for each cross-set, and the dotted orange lines indicate the
 816 10th–90th percentile range of T_t values reconstructed for each cross-set, which we offer as
 817 plausible spreads of values for mean T_t (see Supplementary Methods). Grey shaded region
 818 indicates T_t values of 1–10 days; for the Castlegate Sandstone and Blackhawk Formation, ~90–
 819 95% of median T_t values fall within this range and, for the Ferron Sandstone, ~70% of median
 820 T_t values fall within this range. [1 column figure]



821

822 **Figure 8:** Turnover timescales, T_t , reconstructed for the Castlegate Sandstone, Blackhawk
 823 Formation and Ferron Sandstone using a range of preservation ratios. For these purposes, the
 824 mean cross-set height (h_{xs}) and median grain-size (D_{50}) for each geologic formation have been
 825 used (i.e., the mean and median across all measured cross-set distributions). The solid orange
 826 line indicates the median T_t reconstructed for each bedform preservation ratio, the dashed
 827 orange lines indicate the 25th–75th percentile range of T_t values reconstructed for each
 828 bedform preservation ratio, and the dotted orange lines indicate the 10th–90th percentile
 829 range of T_t values reconstructed for each bedform preservation ratio, which we offer as
 830 plausible spreads of values for mean T_t (see Supplementary Methods). The grey region
 831 highlights the range of median T_t values associated with a plausible range of bedform
 832 preservation ratios; steady-state bedform preservation ratios are ~ 0.3 , and Leary and Ganti
 833 (2020) documented that higher bedform preservation ratios may extend up to ~ 0.7 during
 834 flash floods. On the right y axis, we show reconstructed prevailing flow durations, T_f , for the
 835 scenario in which T_f is a factor of 10 smaller than the reconstructed bedform turnover
 836 timescale. [2 column figure]

837 **Supplement to *Field evidence for disequilibrium dynamics in preserved fluvial***
838 ***cross-strata: A record of discharge variability or morphodynamic hierarchy?***

839 *Sinéad J. Lyster*^{1*}, *Alexander C. Whittaker*¹, *Elizabeth A. Hajek*² and *Vamsi Ganti*^{3,4}

840 ¹*Department of Earth Science and Engineering, Imperial College London, London, UK.*

841 ²*Department of Geosciences, The Pennsylvania State University, Pennsylvania, USA.*

842 ³*Department of Geography, University of California Santa Barbara, California, USA.*

843 ⁴*Department of Earth Science, University of California Santa Barbara, California, USA.*

844 **s.lyster17@imperial.ac.uk*

845 **Contents:**

846 **S1. Field localities**

847 **S2. Extended methodology: Estimation of bedform turnover timescale**

848 **S3. Constraints on bedform preservation ratios**

849 **S4. Data tables**

850

851 **S1. Field localities**

852

853 **Table S1:** *Field localities visited in this study. Localities are grouped by field area (e.g., Price*
854 *Canyon, Wattis Road; see Figure 1 in main text) and subdivided by formation (i.e., Blackhawk*
855 *Formation, Castlegate Sandstone and Ferron Sandstone).*

856

Location and stratigraphic interval		Field sites	Elevation, m ($\pm 3-4$)
Last Chance Creek	Ferron Sandstone	N38 40 18.9, W111 24 52.5	2255
		N38 40 20, W111 24 45.3	2241
		N38 40 21.7, W111 24 17.1	2218
		N38 40 17.5, W111 24 12	2209
		N38 40 12, W111 24 2.5	2190
		N38 40 7.7, W111 23 50.3	2179
		N38 40 9.1, W111 23 44.8	2187
		N38 40 8.9, W111 23 53.6	2215

Link Canyon	Blackhawk Formation	N38 57 42.1, W111 19 57.4	2363
		N38 57 39.7, W111 19 53.9	2383
		N38 57 41.4, W111 19 53.0	2398
		N38 57 44.3, W111 19 53.8	2421
		N38 57 48.4, W111 19 53.9	2473
		N38 57 58.3, W111 19 57.3	2538
		N38 57 52.8, W111 19 55.8	2509
		N38 57 51.4, W111 19 55.0	2500
	Castlegate Sandstone	N38 58 05.9, W111 19 56.6	2572
		N38 58 08.0, W111 19 55.8	2584
		N38 58 10.6, W111 19 54.2	2600
Price Canyon	Blackhawk Formation	N39 44 11.0, W110 50 47.7	1932
		N39 44 08.4, W110 50 46.9	1947
	Castlegate Sandstone	N39 45 05.1, W110 53 10.3	1920
		N39 44 48.5, W110 49 58.1	1969
		N39 44 52.6, W110 49 55.4	1983
		N39 45 01.3, W110 49 43.5	2000
		N39 45 03.0, W110 49 40.6	1999
		N39 45 10.5, W110 49 35.8	2008
N39 45 12.0, W110 49 34.8	2003		
Salina Canyon	Blackhawk Formation	N38 54 00.8, W111 39 53.8	1861
		N38 53 51.5, W111 39 02.3	1885
		N38 54 29.6, W111 41 46.8	1802
		N38 54 13.8, W111 39 05.9	1926
	Castlegate Sandstone	N38 54 52.9, W111 38 06.5	2036
		N38 54 52.3, W111 38 08.7	2017
		N38 54 50.6, W111 38 18.1	2009
		N38 54 52.6, W111 38 20.2	2030
N38 54 53.7, W111 38 ~20.2		2035	
N38 54 33.0, W111 42 32.7		1779	
N38 54 57.1, W111 38 20.3		2076	
N38 54 59.4, W111 38 13.1	2111		

Straight Canyon	Blackhawk Formation	N39 1656.6, W111 1358.0	2027
		N39 1646.2, W111 1341.9	2010
		N39 1629.1, W111 13 11.9	1996
		N39 1716.2, W111 1437.5	2047
		N39 1715.7, W111 1430.4	2043
		N39 1705.7, W111 14 10.5	2037
		N39 1736.5, W111 1616.7	2146
		N39 1719.3, W111 1600.0	2129
		N39 1720.9, W111 1519.8	2102
	Castlegate Sandstone	N39 17 51.9, W111 16 18.0	2161
		N39 18 28.6, W111 16 13.2	2181
		N39 18 55.2, W111 16 06.2	2238
Wattis Road	Blackhawk Formation	N39 31 45.5, W111 02 16.0	2577
		N39 31 11.9, W111 0156.9	2692
		N39 31 19.8, W111 0158.4	2655
		N39 31 20.7, W111 0237.2	2798
		N39 31 14.3, W111 0213.8	2765
	Castlegate Sandstone	N39 31 28.6, W111 02 44.9	2844
		N39 31 31.7, W111 0250.6	2877
		N39 31 30.2, W111 0246.4	2861
		N39 31 33.5, W111 02 53.2	2889
Willow Basin	Ferron Sandstone	N38 3450.9, W111 28 6.2	2668
		N38 3449, W111 28 6.5	2636
		N38 3448.9, W111 28 4.5	2631
		N38 3447.6, W111 28 5.4	2592
		N38 3435.1, W111 27 48.4	2537
Willow Creek	Ferron Sandstone	N38 440.4, W111 18 47.2	1965
		N38 4337.4, W111 18 46.5	1926
		N38 4325.2, W111 18 45.9	1895

857

858

859 **S2. Extended methodology: Estimation of bedform turnover timescale**

860 We propagated mean thicknesses of individually measured cross-sets (and their respective
861 grain-sizes) through a well-established quantitative framework (c.f. Ganti et al., 2019; Lyster
862 et al., 2021) to reconstruct a variety of palaeohydraulic parameters and, eventually, bedform

863 turnover timescales, T_t . We first reconstructed mean original bedform (i.e., dune) height, h_d ,
864 as a function of mean cross-set thickness, h_{xs} , using the relation of Leclair and Bridge (2001),

$$h_d = 2.9(\pm 0.7)h_{xs}, \quad [\text{Eq. S1}]$$

865 where 2.9 is the mean (μ) and 0.7 is the standard deviation (σ). The above relation was
866 experimentally derived for steady-state conditions, i.e., bedform preservation ratio (h_{xs}/h_d) of
867 ~ 0.3 . However, bedform preservation in disequilibrium conditions may imply that h_{xs}/h_d is
868 higher (Jerolmack & Mohrig, 2005; Reesink et al., 2015; Ganti et al., 2020; Leary & Ganti,
869 2020). Initially, we assumed h_{xs}/h_d of ~ 0.3 , which means that T_t estimates are maximum
870 values. We subsequently evaluated the sensitivity of T_t to h_{xs}/h_d (see Methods in main text).
871 Finally, we estimated likely values of h_{xs}/h_d for each geologic formation using available data
872 (Section S3), which broadly range from 0.3–0.7, and used these values to contextualise the
873 implications of this sensitivity on our results (Figure 8 in main text).

874 We used a Monte Carlo uncertainty propagation method to estimate uncertainty (c.f. Lyster
875 et al., 2021). In doing so, we offer plausible spreads of values for the median of each
876 reconstructed parameter. From Equation S1, we generated 10^6 random samples of the model
877 parameter between bounds defined by $\mu - \sigma$ and $\mu + \sigma$. To avoid introduction of additional
878 assumptions, we generated these samples from a uniform distribution as the shape and the
879 scale of the full distribution of the data is unknown. These 10^6 samples were used to calculate
880 10^6 values of h_d , and these results were propagated through subsequent calculations. Given
881 that Equation S1 assumes steady-state flow conditions and a h_{xs}/h_d value of ~ 0.3 , and that we
882 randomly sampled the model parameter between $\mu - \sigma$ and $\mu + \sigma$, we note that our uncertainty
883 analysis analytically accounts for some variability in h_{xs}/h_d , between ~ 0.28 and ~ 0.45 .

884 To reconstruct formative flow depth, H , we used the bedform height–flow depth scaling
885 relation of Bradley and Venditti (2017), which was derived using >380 empirical data. Bradley
886 and Venditti (2017) presented a non-parametric relation which characterized their data,
887 which did not assume an underlying distribution for the scaling parameter. In this relation,
888 median H is given as

$$H = 6.7h_d, \quad [\text{Eq. S2}]$$

889 with a probabilistic uncertainty estimator in which the 1st and 3rd quartiles of H are given by
890 $H=4.4h_d$ and $H=10.1h_d$, respectively (Bradley & Venditti, 2017). We generated 10^6 random
891 samples between 4.4 and 10.1, again from a uniform distribution, and reconstructed 10^6
892 values of H in these ancient fluvial systems using Equation S2. These values were then used
893 to estimate bedform wavelength, λ , as $\lambda=7.3H$, following van Rijn (1984).

894 To reconstruct palaeoslope, we used the empirical method of Trampus et al. (2014).
 895 Palaeoslopes may also be calculated by a Shields stress inversion where the dimensionless
 896 Shields stress is known (or where it can be estimated using, e.g., bedform stability diagrams;
 897 Carling (1999)). However, we implemented the method of Trampus et al. (2014) for
 898 consistency with the method that Mahon and McElroy (2018) used to derive Equations S4 and
 899 S5. In addition, previous studies have shown that both palaeoslope methods recover similar
 900 values for sand-grade grain-sizes (Ganti et al., 2019; Lyster et al., 2021). Trampus et al. (2014)
 901 expressed palaeoslope, S , as

$$\log S = \alpha_0 + \alpha_1 \log D_{50} + \alpha_2 \log H, \quad [\text{Eq. S3}]$$

902 where $\alpha_0 = -2.08 \pm 0.036$, $\alpha_1 = 0.254 \pm 0.016$, and $\alpha_2 = -1.09 \pm 0.044$ are constants. We randomly
 903 sampled 10^6 values of α_0 , α_1 , and α_2 (uniformly distributed between $\mu - \sigma$ and $\mu + \sigma$) and
 904 reconstructed 10^6 values of S .

905 To calculate characteristic bedform migration velocity, V_c , and therefore unit bedload flux, q_b ,
 906 we used the bedform-scale (as opposed to grain-scale) approach of Mahon and McElroy
 907 (2018), in which q_b is estimated geometrically, per unit width, as a function of bedform
 908 migration velocity, V_c . These variables are given as:

$$\log V_c = \beta_0 + \beta_1 \log S, \quad [\text{Eq. S4}]$$

$$q_b = (1 - \varphi) \frac{h_d V_c}{2}, \quad [\text{Eq. S5}]$$

909 where $\beta_0 = 0.6113 \pm 0.144$ and $\beta_1 = 1.305 \pm 0.0515$ are constants, and φ is a dimensionless bed
 910 porosity of 0.5 (Mahon & McElroy, 2018). To reconstruct V_c , we randomly sampled 10^6 values
 911 for the model parameters, β_0 and β_1 , from a uniform distribution between bounds defined by
 912 $\mu - \sigma$ and $\mu + \sigma$. These values were then used to estimate q_b (Equation S5).

913 Having calculated 10^6 values of h_d , H , λ , S , V_c , and q_b , we reconstructed bedform turnover
 914 timescales, T_t , i.e., the time taken to displace the volume of sediment of the bedform (per
 915 unit width), following Martin and Jerolmack (2013) and Myrow et al. (2018), as:

$$T_t = \frac{\lambda h_d \beta}{q_b}, \quad [\text{Eq. S6}]$$

916 where $\beta \sim 0.55$ is the bedform shape factor.

917 This recovered 10^6 values of T_t in units of seconds which we converted to days. From these
 918 values, we extracted median T_t , the 25–75 percentile range of T_t (or the 1st–3rd interquartile

919 range of T_t), and the 10–90 percentile range of T_t . Given that the errors and uncertainties
920 associated with Equations S2–S6 are propagated through the methodology, and that these
921 errors and uncertainties are compounded on top of each other, we suggest that the 10–90
922 percentile range of T_t offers plausible minimum and maximum values for median T_t , with the
923 25–75 percentile range of T_t highlighting where true values of median T_t are most likely to
924 occur between these bounds.

925 **S3. Constraints on bedform preservation ratios**

926 As discussed in the main text, and above, the scaling relation of Leclair and Bridge (2001)
927 (Equation S1) is derived for steady-state conditions, which implies that reconstructed H values
928 are also steady-state estimates. However, it is expected that h_{xs}/h_d is higher in disequilibrium
929 conditions (see main text). The ability to constrain h_{xs}/h_d from geological outcrop would be
930 useful for evaluating the nature of bedform preservation, however this is difficult in practice.

931 In order to accurately constrain h_{xs}/h_d , we ideally require systematic measurements of cross-
932 set heights and knowledge of their original bedform heights, however it is not possible to
933 know original bedform heights in ancient fluvial systems. Instead, we can contrast cross-set
934 heights with independent proxies of H , e.g., barform heights. If H values reconstructed from
935 mean cross-set heights using steady-state assumptions agree with independent proxies of H ,
936 then this might imply that h_{xs}/h_d was truly ~ 0.3 . However, this approach requires us to assume
937 the relationship between the original bedform height and the palaeoflow depth (Equation S2)
938 in order to recover a value for h_{xs}/h_d . Reconstructions of h_{xs}/h_d are therefore estimates.
939 Moreover, barform heights are a proxy for maximum bankfull depths which, given the
940 possibility that mean bankfull depths are smaller, will act to decrease the estimated value of
941 h_{xs}/h_d . This is particularly true where the heights of point bar deposits are used as
942 independent proxies of H , as flow depths in meandering systems are typically greater on
943 meander bends. One further issue with this approach is that the barforms themselves may
944 not be fully preserved (Chamberlin & Hajek, 2019).

945 In this study, despite our detailed data collection, we do not have the desired spatiotemporal
946 resolution of field measurements to accurately constrain h_{xs}/h_d , i.e., we do not have a mean
947 cross-set height and the mean height of the associated barform for each measured cross-set.
948 However, as a starting point, we compared mean cross-set heights across our field areas (Fig.
949 1 in main text) with mean barform heights in published literature. Based on stratigraphic
950 observations, detailed below, we predict that values of h_{xs}/h_d likely ranged between 0.3 and
951 0.7. This suggests that uncertainty margins in Equation S1, which analytically account for
952 variability in h_{xs}/h_d between ~ 0.28 and ~ 0.45 , are reasonable. It is unlikely that h_{xs}/h_d is much
953 smaller than ~ 0.3 because, as mentioned in the main text, if h_{xs}/h_d is much smaller than ~ 0.3
954 then T_t rapidly increases from 10^1 to 10^5 days (Eq. S1 and S2), which are implausible bedform
955 migration timescales.

956 We recovered median values of h_{xs} equal to ~ 0.13 – 0.14 m for the Blackhawk Formation and
957 Castlegate Sandstone, but which broadly span 0.1–0.2 m. H values reconstructed using

958 steady-state assumptions have previously been verified for the Blackhawk Formation and
 959 Castlegate Sandstone by Lyster et al. (2021). The authors reconstructed median H values of
 960 2–4 m from cross-sets spanning the Blackhawk Formation and Castlegate Sandstone at
 961 localities along the eastern front of the Wasatch Plateau (Lyster et al., 2021). These H values
 962 are in broad agreement with H values independently inferred from bar-scale clinoform
 963 heights, which have means of ~ 3 –3.5 m, but which typically span 1–8 m (Adams &
 964 Bhattacharya, 2005; Lynds & Hajek, 2006; McLaurin & Steel, 2007; Hajek & Heller, 2012;
 965 Chamberlin & Hajek, 2019; Lyster et al., 2021). Assuming the model parameter in Equation S3
 966 is true, we might expect values of h_{xs}/h_d up to 0.6–0.7.

967 Meanwhile, for the Ferron Sandstone, H values reconstructed using steady-state assumptions
 968 have not previously been verified. Here, from individually measured cross-sets ($n=190$), we
 969 recovered median values of 0.15 m for mean cross-set heights, which broadly span 0.1–0.3
 970 m. Using Equation S3 we project median values for H of ~ 3 m, but which broadly span 1–10
 971 m (Equation S3). Independent proxies of H are limited for the Ferron Sandstone. As such, in
 972 the field we obtained new measurements of independent H proxies, e.g., laterally accreted
 973 point bar deposit heights, which we made using a Haglof Laser Geo laser range finder to a
 974 precision of ± 5 cm, and which we used to supplement limited secondary data (Table S2). In
 975 the Ferron Sandstone, previous work has documented channel-fill deposits and laterally
 976 accreted point bars with heights of order 8–9 m (Cotter, 1971; Gardner et al., 2004; Garrison
 977 & Bergh, 2004). Here we report a broader range of heights for independent H proxies (Table
 978 S2). Across 35 measurements of point bar/lateral accretion set heights (Table S2), we recover
 979 a mean height of 4.7 m, with a 1st–3rd interquartile range spanning 2.9–6.5 m. Minimum and
 980 maximum heights are 1.1 and 10 m, respectively (Table S2). Similarly, if we assume the model
 981 parameter in Equation S3 is true, then we might expect h_{xs}/h_d values up to 0.6–0.7.

982 **Table S2: Independent measurements of palaeoflow depth indicators in the Ferron Sandstone**

Palaeoflow depth proxy	Thickness (m)	Source
Laterally accreted point bar deposit	9.1	Cotter (1971)
Laterally accreted point bar deposit	<8	Gardner et al. (2004)
Maximum thickness of channel-fill deposits	~ 9	Gardner et al. (2004)
Maximum thickness of channel-fill deposits	~ 9	Garrison and Bergh (2004)
Laterally accreted point bar deposits	8, 7.5, 9, 3.2, 4.8, 3.6, 6.5, 7.5, 3.6, 4.1, 2.7, 6.4, 5.5, 2.8, 1.1, 1.9, 7.5, 2.7, 7.1, 1.2, 4.4, 3.7, 3.1, 3.4, 3, 2.5, 5.9, 2.5, 4.7, 10, 4.2, 1.6, 3, 6.5, 10	This study

Maximum thickness of single channel storeys	8.6, 11.1, 12.2, 9, 7.6, 7.1, 3.9, 5.6, 2.6, 7.3, 12, 9.3	This study
--	---	-------------------

983

984 **S4. Data tables**

985 We provide a Microsoft Excel spreadsheet containing field results and a selection of
 986 reconstructed palaeohydrologic parameters for the Blackhawk Formation, Castlegate
 987 Sandstone and Ferron Sandstone. Field data and results are reported per field area (see Fig.
 988 1 in main text).

989

990 **Supplementary references**

- 991 Adams, M. M., & Bhattacharya, J. P. (2005). No change in fluvial style across a sequence boundary,
 992 Cretaceous Blackhawk and Castlegate formations of central Utah, U.S.A. *Journal of*
 993 *Sedimentary Research*, 75(6), 1038-1051. doi:10.2110/jsr.2005.080
- 994 Bradley, R. W., & Venditti, J. G. (2017). Reevaluating dune scaling relations. *Earth-Science Reviews*,
 995 165, 356-376. doi:10.1016/j.earscirev.2016.11.004
- 996 Carling, P. A. (1999). Subaqueous gravel dunes. *Journal of Sedimentary Research*, 69(3), 534-545.
 997 doi:10.2110/jsr.69.534
- 998 Chamberlin, E. P., & Hajek, E. A. (2019). Using bar preservation to constrain reworking in channel-
 999 dominated fluvial stratigraphy. *Geology*, 47(6), 531-534. doi:10.1130/G46046.1
- 1000 Cotter, E. (1971). Paleoflow characteristics of a late Cretaceous river in Utah from analysis of
 1001 sedimentary structures in the Ferron sandstone. *Journal of Sedimentary Research*, 41, 129–
 1002 138. doi:10.1306/74D72202-2B21-11D7-8648000102C1865D
- 1003 Ganti, V., Hajek, E. A., Leary, K., Straub, K. M., & Paola, C. (2020). Morphodynamic hierarchy and the
 1004 fabric of the sedimentary record. *Geophysical Research Letters*, 47(14), e2020GL087921.
 1005 doi:10.1029/2020GL087921
- 1006 Ganti, V., Whittaker, A., Lamb, M. P., & Fischer, W. W. (2019). Low-gradient, single-threaded rivers
 1007 prior to greening of the continents. *Proceedings of the National Academy of Sciences*, 116(4),
 1008 11652-11657. doi:10.1073/pnas.1901642116
- 1009 Gardner, M. H., Cross, T. A., & Levorsen, M. (2004). Stacking Patterns, Sediment Volume Partitioning,
 1010 and Facies Differentiation in Shallow-Marine and Coastal-Plain Strata of the Cretaceous
 1011 Ferron Sandstone, Utah. In T. C. Chidsey, Jr., R. D. Adams, & T. H. Morris (Eds.), *Regional to*
 1012 *Wellbore Analog for Fluvial-Deltaic Reservoir Modeling: The Ferron Sandstone of Utah* (Vol.
 1013 50, pp. 0): American Association of Petroleum Geologists. doi:10.1306/St50983
- 1014 Garrison, J. R., Jr., & Bergh, T. C. V. v. d. (2004). High-Resolution Depositional Sequence Stratigraphy
 1015 of the Upper Ferron Sandstone Last Chance Delta: An Application of Coal-Zone Stratigraphy.
 1016 In T. C. Chidsey, Jr., R. D. Adams, & T. H. Morris (Eds.), *Regional to Wellbore Analog for*
 1017 *Fluvial-Deltaic Reservoir Modeling: The Ferron Sandstone of Utah* (Vol. 50, pp. 0): American
 1018 Association of Petroleum Geologists. doi:10.1306/St50983
- 1019 Hajek, E. A., & Heller, P. L. (2012). Flow-depth scaling in alluvial architecture and nonmarine
 1020 sequence stratigraphy: Example from the Castlegate Sandstone, central Utah, U.S.A. *Journal*
 1021 *of Sedimentary Research*, 82(2), 121-130. doi:10.2110/jsr.2012.8

1022 Jerolmack, D. J., & Mohrig, D. (2005). Frozen dynamics of migrating bedforms. *Geology*, 33(1), 57-60.
1023 doi:10.1130/G20897.1

1024 Leary, K. C. P., & Ganti, V. (2020). Preserved fluvial cross strata record bedform disequilibrium
1025 dynamics. *Geophysical Research Letters*, 47(2), e2019GL085910. doi:10.1029/2019GL085910

1026 Leclair, S. F., & Bridge, J. S. (2001). Quantitative interpretation of sedimentary structures formed by
1027 river dunes. *Journal of Sedimentary Research*, 71(5), 713-716. doi:1527-1404/01/071-
1028 713/\$03.00

1029 Lynds, R., & Hajek, E. (2006). Conceptual model for predicting mudstone dimensions in sandy
1030 braided-river reservoirs. *AAPG Bulletin*, 90(8), 1273-1288. doi:10.1306/03080605051

1031 Lyster, S. J., Whittaker, A. C., Hampson, G. J., Hajek, E. A., Allison, P. A., & Lathrop, B. A. (2021).
1032 Reconstructing the morphologies and hydrodynamics of ancient rivers from source to sink:
1033 Cretaceous Western Interior Basin, Utah, USA. *Sedimentology*. doi:10.1111/sed.12877

1034 Mahon, R. C., & McElroy, B. (2018). Indirect estimation of bedload flux from modern sand-bed rivers
1035 and ancient fluvial strata. *Geology*, 46(7), 579-582. doi:10.1130/G40161.1

1036 Martin, R. L., & Jerolmack, D. J. (2013). Origin of hysteresis in bed form response to unsteady flows.
1037 *Water Resources Research*, 49(3), 1314-1333. doi:10.1002/wrcr.20093

1038 McLaurin, B. T., & Steel, R. J. (2007). Architecture and origin of an amalgamated fluvial sheet sand,
1039 lower Castlegate Formation, Book Cliffs, Utah. *Sedimentary Geology*, 197(3), 291-311.
1040 doi:10.1016/j.sedgeo.2006.10.005

1041 Myrow, P. M., Jerolmack, D. J., & Perron, J. T. (2018). Bedform disequilibrium. *Journal of*
1042 *Sedimentary Research*, 88(9), 1096-1113. doi:10.2110/jsr.2018.55

1043 Reesink, A. J. H., Van den Berg, J. H., Parsons, D. R., Amsler, M. L., Best, J. L., Hardy, R. J., Orfeo, O., &
1044 Szupiany, R. N. (2015). Extremes in dune preservation: Controls on the completeness of
1045 fluvial deposits. *Earth-Science Reviews*, 150, 652-665. doi:10.1016/j.earscirev.2015.09.008

1046 Trampus, S. M., Huzurbazar, S., & McElroy, B. (2014). Empirical assessment of theory for bankfull
1047 characteristics of alluvial channels. *Water Resources Research*, 50(12), 9211-9220.
1048 doi:10.1002/2014WR015597

1049 van Rijn, L. C. (1984). Sediment transport III: bedforms and alluvial roughness. *Journal of Hydraulic*
1050 *Engineering*, 110(12), 1733-1754. doi:10.1061/(ASCE)0733-9429(1984)110:12(1733)

1051